Synthesis of Fe and Cu co-doped ZnO Nanocomposite (ICZ-Cs) for Catalytic Activity of Methylene Blue and 4-nitrophenol dyes from Aqueous Solution

Hiwot Belay Kassa

A Thesis Submitted to Department of Applied Chemistry
School of Applied Natural Science

Presented in Partial Fulfillment of the Requirement for the Degree of Master's of Science in Applied Chemistry (Specialization in Industrial Chemistry)

Office of Post Graduate Studies
Adama Science and Technology University

June, 2023
Adama, Ethiopia

Synthesis of Fe and Cu co-doped ZnO Nanocomposite (ICZ-Cs) for Catalytic Activity of Methylene Blue and 4-nitrophenol dyes from Aqueous Solution

Hiwot Belay Kassa

Advisor: Buzuayehu Abebe (PhD)

Co-Advisor: Dereje Tsegaye (PhD)

A Thesis Submitted to Department of Applied Chemistry

School of Applied Natural Science

Presented in Partial Fulfillment of the Requirement for the Degree of Master's of Science in Applied Chemistry (Specialization in Industrial Chemistry)

Office of Post Graduate Studies

Adama Science and Technology University

June, 2023

Adama, Ethiopia

DECLARATION

I declare that this thesis work entitled **"Synthesis of Fe and Cu co-doped ZnO Nanocomposite (ICZ-Cs) for Catalytic Activity of Methylene Blue and 4-nitrophenol dyes from Aqueous Solution"** is my own work and has not been submitted to any university for a similar purpose. The references used in this thesis are duly recognized by proper citations.

_____ _____ _____

Name of Student Signature Date

RECOMMENDATION OF ADVISOR

We the advisors of this thesis, hereby certify that We have closely advised/supervised the student while developing this thesis and read the revised version of thesis work entitled **"Synthesis of Fe and Cu co-doped ZnO Nanocomposite (ICZ-Cs) for Catalytic Activity of Methylene Blue and 4-nitrophenol dyes from Aqueous Solution"** prepared under our guidance by Hiwot Belay Kassa. Therefore, we recommend the submission of the thesis to the department for further review and evaluation.

_____	_____	_____
Major Advisor	Signature	Date
_____	_____	_____
Co – Advisor	Signature	Date

APPROVAL

We the advisors of the thesis entitled "**Synthesis of Fe and Cu co-doped ZnO Nanocomposite (ICZ-Cs) for Catalytic Activity of Methylene Blue and 4-nitrophenol dyes from Aqueous Solution"** and developed by Hiwot Belay Kassa, hereby certify that the recommendation and suggestions made by the board of examiners are appropriately incorporated into the final version of the thesis.

_____	_____	_____
Major Advisor	Signature	Date
_____	_____	_____
Co – Advisor	Signature	Date

APPROVAL OF BOARD OF REVIEWERS

We, the undersigned, members of the Board of Reviewers of the thesis open defense by Hiwot Belay Kassa have read and evaluated the thesis work **"Synthesis of Fe and Cu co-doped ZnO Nanocomposite (ICZ-Cs) for Catalytic Activity of Methylene Blue and 4-nitrophenol dyes from Aqueous Solution"** and assessed the understanding of the candidate about the proposed research. This is, therefore, to certify that the thesis is accepted and we recommend the implementation of the thesis.

_____	_____	_____
Chairperson	Signature	Date
_____	_____	_____
Reviewer 1	Signature	Date
_____	_____	_____
Reviewer 2	Signature	Date

Finally, approval and acceptance of the thesis are contingent upon the submission of its final copy to the Office of Postgraduate Studies (OPGS) through the Department Graduate Council (DGC) and School Graduate Committee (SGC).

_____	_____	_____
Department Head	Signature	Date
_____	_____	_____
School Dean	Signature	Date
_____	_____	_____

ACKNOWLEDGEMENT

First, I would like to thank God the almighty, for letting me through all the difficulties. I have experienced your guidance day by day. You are the one who let me finish my work. I am sincerely express my gratitude to Dr. Hoden Ali Farah for letting me study the master's program in ASTU by recompense my full tuition fee and funding financial support and research fund to accomplish this research. I also acknowledge Adama Science and Technology University (ASTU) and Dr. Dereje Teklu for giving me the chance of MSc opportunity. I would like to express my sincere gratitude to my advisor Dr. Buzuayehu Abebe who made this work possible by bringing his considerable experience and knowledge to this project. His guidance and advise carried me through all the stages of doing my work and writing my thesis, I am extremely grateful for your assistance and suggestion throughout my project. I am very grateful for my co-advisor Dr. Dereje Tsegaye. I would also to say thanks to Dr. H.C Ananda Murthy, Mr. Demeke Tesfaye and Mr. Guta Amenu for their encouragement and support. Finally, I would like to give my warmest thanks to my family and friends for their continuous support and understanding when undertaking my project, your prayer helps me survive all the stress from this year and not letting me give up.

TABLE OF CONTENTS

LIST OF TABLES

LIST OF FIGURES

LIST OF ACRONYMS

AHS	High-temperature synthesis
AOPs	Advanced oxidative processes
CB	Conduction band
CS	critical supersaturation level
DTA	differential thermal analysis
EDX	Energy Dispersive X-ray
Eg	energy gap
FESEM	Field Emission Scanning Electron Microscope
FTIR	Fourier Transform Infrared Spectroscopy
HRTEM	Higher Resolution Transmission Electron Microscope
ICZ-Cs	Fe- and Cu co-doped ZnO-composites
NBE	near-band edge
NaOH	Sodium hydroxide
NCs	Nano composites
NPs	Nanoparticles
PL	Photoluminescence spectroscopy
PVA	Poly (vinyl) alcohol
PVP	Polyvinyl pyridine
SAED	Selected area Electron Diffraction
TEM	Transmission Electron Microscopy
TGA	Thermal Gravimetric Analysis
UV-VIS- DRS	Ultraviolet-visible diffuse reflectance
VB	Valence band
XRD	X-ray diffractometer

Abstract

Stable nanomaterials with enhanced light absorption and synergistic effects are crucial for pollutant remediation. The Fe and Cu co-doped ZnO nanocomposites in this study were synthesized by the auto-combustion high-temperature synthesis (AHS) approach for the removal of methylene blue (MB) and 4-nitrophenol (4-NP) dyes from aqueous solution. . The TGA-DTA was used for thermal analysis. The result showed 490 °C as the point at which stable metal oxide is formed. XRD was used for crystalline size determination. The XRD pattern analysis not revealed the perfect iron and copper inclusion in the ZnO lattice at lower dopant concentrations and the formation of a CuO-independent peak at higher concentrations. An enhanced crystallite size increment of 10–26 nm was observed with increasing calcination time from 30 min to 3h. The porosity occurred during gas evolution, and dispersed nanoparticles were clearly observed on the FESEM images. The EDX compositional analysis confirmed the presence of only expected elements without impurities, in perfect proportion, and in accordance with the amount used during synthesis. The elemental mapping analysis confirms the good dopant distribution on the ZnO surface. FESEM/TEM provided the rod and spherical forms of the morphology. SAED and XRD results supported ZnO NP and ICZ-C15 crystallinity. From the HRTEM image and XRD pattern analysis, a minor lattice fringe difference value between ZnO and ICZ-C15 was confirmed. A greater PL intensity reduction for the composites than ZnO confirms the presence of electron-hole recombination hindrance due to doping. Dopant inclusion in the ZnO lattice resulted in the composite having higher light absorption properties and a redshift on the DRS-UV-VIS analysis when compared to bare ZnO. Besides, the formation of ZnO-CuO heterojunction is also beneficial for photon-induced electron-hole recombination hindrance properties. Because of their higher light absorption properties and synergistic effect, the doped nanocomposites outperformed ZnO in 4-nitrophenol and methylene blue catalysis. 82.25 and 99.135 of performance ICZ-C15 was obtained in reduction of MB and 4-NP respectively. 90.23% of degradation of MB was performed in ICZ-C15 as compared to ZnO, ICZ-C1, and ICZ-C10. As a result, the AHS approach provides a comprehensive outlook for future environmental safety applications.

Keywords: *Photocatalyst, zinc oxide, co-doping, Methylene Blue, and 4-nitrophenol*

CHAPTER ONE

1. Introduction

1.1. Background of the study

Environmental contamination has recently caused significant socioeconomic problems in human society. It has been discovered that wastewater contains colors from many companies, contaminating the water. Dye usage in excess can be harmful to human health. More than 7 x 10^5 tons of these dyes and pigments are produced each year, and 5 - 15% of that amount is lost in industrial effluents (Irani et al., 2016). The main causes of pollution in the textile industry are the dyeing and finishing procedures. Due to their resistance to oxidizing agents and slow or incomplete breakdown, dyes are difficult to remove from wastewater, which causes some environmental issues (Kowsari, 2017). After being released into the aquatic ecosystem, organic pollutants can cause a variety of environmental issues, including reduced light penetration, reduced photosynthesis, and harmful effects on aquatic biota. Among the many organic pollutants, the cationic dye methylene blue, which is primarily employed as a colorant in the paper, rubber, and textile industries, causes adverse effects. Methylene blue (MB), a cationic thiazine dye, is water-soluble, has a blue color, and is toxic (Duan et al., 2022). In the presence of a reducing agent and catalysts, MB undergoes redox reduction (clock reaction), first to leucomethylene blue (LMB), and then back to MB due to the low stability of LMB in the aerated condition (Basu et al., 2012). Besides, the toxic nitroaromatic compound, 4-nitrophenol (4-NP), which is used as an intermediate ingredient in different fields like leather and pharmaceutical industry, is also easily reduced to the less toxic 4-aminophenol (4-AP) in the presence of a reducing agent and catalyst (Bagheri et al., 2022; Mejía & Reddy Bogireddy, 2022).

To remove organic dyes and pigments from wastewater, physical, chemical, and biological techniques are being applied. Adsorption, coagulation, and membrane separation, among other conventional procedures, have been proven to be very expensive and cause secondary pollution. Advanced oxidative processes (AOPs), which include photocatalysis, the Fenton reaction, and ozonation, have been utilized effectively to eliminate organic pollutants. Because of its effectiveness, adaptability, convenience, simplicity, low cost, and environmentally sound approach for treating pollutants, the photocatalytic degradation method—which combines a semiconductor with UV light—is receiving increased attention. Being able to convert pollutants into less harmful substances like CO_2 and H_2O is another

benefit of photocatalysis (Chen et al., 2000). Heterogeneous photocatalysis with various metal oxides and semi-conducting catalysts (ZnO, CdS, TiO_2, Fe_2O_3, and ZnS) and related compounds proved to be a highly efficient solution for the degradation of organic pollutants. Heterogeneous photocatalysis results in the complete mineralization of intermediate chemicals, which decreases the danger of secondary contamination and reduces operating costs. The use of nanotechnology-assisted synthesized nanoscale materials is now spreading throughout the universe in different fields of study due to the possibilities of creating materials with novel properties and applications (Andreo et al., 2022). During the massive industrial revolution, the development of catalysis technology was reported as basic science for the removal of pollutants (Mitchell et al., 2021). ZnO is one of the broader bandgap materials that has a large excitation binding energy of 60 meV and is environmentally friendly and cost-effective (Khan et al., 2020). However, it has catalytic drawbacks, including a low surface area and photon-induced electron-hole recombination. Besides, ZnO is a high-bandgap semiconductor material, which is not desirable for catalytically degrading pollutants under sunlight illumination (Nadeem et al., 2021).

The doping and local contact/heterojunction strategies are receiving attention to avoid the mentioned ZnO drawbacks (Tsogoo et al., 2023). The doping of metal ions in the ZnO lattice induces photon-induced electron trapping sites. The created site has great effects on improving the optoelectrical properties of ZnO and also augments its visible light absorption potential (Naseer et al., 2022). Copper is one of the low bandgap materials (2.2 eV) that has less toxic properties, good photoactivity, and is abundant (Ali et al., 2022). According to reports, heterojunction is important in the different phases of copper oxides: Cu-CuO-Cu_2O, for facilitating charge separation efficiency and extending photoexcitation energy (Lupan et al., 2020; Uthirakumar et al., 2020). The broad bandgap of ZnO can be tuned by doping Cu(II) or Cu(I), which creates a deep acceptor level at about 0.17 eV, slightly below the ZnO conduction band, resulting in tuning ZnO optical properties (Agarwal et al., 2019). The alpha-phase iron oxide (α-Fe_2O_3) is a direct bandgap material (2.2 eV), which is handy, non-toxic, and has a noble visible-light absorption capacity (Zhao et al., 2021). The doping of iron in the ZnO host lattice increases the host's stability (Khan et al., 2020). The doping of iron in the ZnO lattice also creates a charge imbalance due to the small ionic radius of iron (III) (0.06 nm) compared to the zinc (II) ionic radius (0.074 nm) (Nadeem et al., 2021).

Heterogeneous catalyst-based environmental remediation research, specifically the inclusion of iron and copper in the ZnO lattice as well as the formation of heterojunction, has been extensively reported. Khan et al. synthesized Fe^{3+}-doped ZnO composites by a modified sol-gel method. The X-ray diffraction (XRD) pattern analysis showed only the hexagonal wurtzite structure of ZnO up to 1% iron dopant amount, without an independent peak for iron. Here, the absence of an iron secondary peak on the XRD pattern is due to its total inclusion in the ZnO lattice (Khan et al., 2020). Samanta et al. also used the sol-gel method to create iron-doped ZnO with a maximum iron content of 15%. According to the XRD pattern analysis, here too the pattern showed only for the hexagonal wurtzite structure of ZnO. The absence of an independent iron peak as well as intensity reductions with an increase in iron content were reported to be due to the well-inclusion of iron in the host lattice (Samanta et al., 2020). The single-phase iron-doped ZnO synthesised by solution combustion synthesis was also reported in the Dhiman et al. study. In this study, an intensity reduction and a higher-angle peak shift were observed due to iron doping in the ZnO lattice (Dhiman et al., 2017).

Besides, in the Tsogoo et al. study, the solvothermal method was used for synthesizing Cu-doped ZnO nanocomposites (NCs) in the presence of benzyl alcohol as a reducing agent of copper ions to copper metal. Increasing the copper concentration resulted in the formation of a copper metal-independent peak. There is also a lower angle shift (a greater d-spacing value) due to internal strain and a peak broadening on the XRD pattern with an increase in the concentration of dopant compared to the bare ZnO. The bandgap narrowed from 3.32 eV to 3.28 eV, which confirms the inclusion of copper in the ZnO lattice. The occurrence of an independent peak for copper at lower concentrations confirms its lower solubility behaviour in the ZnO lattice (Tsogoo et al., 2023). Agarwal et al. synthesized Cu-doped ZnO up to a 15% dopant concentration using the atomic beam co-sputtering technique. Here in this study, the ZnO lattice distortion occurred beyond a 3% copper amount, and the occurrence of the copper-independent peak was above 7% within the instrument's minimum detection limit. Of course, the redshift on Tauc's plot analysis for 15% doped NCs showed a bandgap reduction of up to 2.8 eV, compared to the ZnO that has a bandgap of 3.4 eV (Agarwal et al., 2019). Mahmoud (Mahmoud et al., 2021) and Morales-Mendoza with their groups (Morales-Mendoza & Paraguay-Delgado, 2021) synthesised the copper-doped ZnO composite and showed the formation of copper-independent peaks above 4 and 6 copper dopant percentages, respectively. Recently, Zverev et al. also synthesised 5% iron-doped

and 5% copper-doped ZnO independently using the combustion synthesis approach. In this work, the occurrence of a copper-independent peak in copper-doped ZnO and the absence of an iron-independent peak in iron-doped ZnO were reported. The absence of an independent peak for iron was due to its inclusion in the zinc oxide lattice (Zverev et al., 2022).

Moreover, doping with more than one type of element has received great interest as it can have synergistic effects on the targeted applications (Subash et al., 2012). Some reports (Shim et al., 2005; Tiwari et al., 2017; Viswanatha et al., 2012) synthesised the Fe- and Cu-co-doped ZnO-composite (ICZ-C) only for the magnetic properties study. Shim et al. (Shim et al., 2005) confirmed the ferromagnetic properties of the ICZ-C to be a result of the $ZnFe_2O_4$ secondary phase. Viswanatha et al. (Viswanatha et al., 2012) confirmed the ferromagnetic properties of ICZ-C as a result of a double exchange between different Fe oxidation states in the presence of copper ($Fe^{2+} + Cu^{2+} \rightarrow Fe^{3+} + Cu^{+}$). In the contrary, Tiwari et al. (Tiwari et al., 2017) reported an increase in the antiferromagnetic properties of ICZ-C with an increase in copper amount. In general, the above iron-doped ZnO and copper-doped ZnO studies reported less solubility for copper and good solubility for iron in the ZnO lattice based on their XRD analyses. However, there is no detailed analysis that confirms the inclusion of iron in the ZnO lattice. This means that the absence of an iron peak on the XRD pattern may also be due to the ZnO dominance within the instrumental detection limit. Regarding the authors' literature survey, there is no report regarding the synthesis of Fe and Cu co-doped ZnO nanocomposites (ICZ-Cs) using the AHS approach.

The nanoscale catalyst synthesis using the AHS has many distinct merits, such as time, energy, and simplicity. Besides, AHS also provides a secondary structure: porous nanocrystal frameworks that have great advantages for several applications, such as catalysis, sensors, and energy devices (Deng et al., 2013). Thus, special attention should be given to nanoscale catalyst synthesis using the AHS approach (Thoda et al., 2018). Under controlled parameters, the source of heat in the AHS is the combustion reaction of the complex formed within the precursor and surfactant or reducing agent (Varma et al., 2016).

Thus, this study focuses on synthesizing ZnO nanoparticles (NPs) and ICZ-Cs using the simple and energy- and time-efficient AHS approach. The synthesised materials showed a highly porous morphology with a noble dopant distribution. The porous nature, composition, and dopant distribution were deduced from the field emission scanning

electron microscopy and energy dispersive x-ray (FESEM-EDX) morphological, compositional, and elemental mapping analyses. The crystallinity, effect of calcination time, doping, and heterojunction properties were deduced from the XRD pattern analysis. The material's thermal stability was witnessed through thermal –gravimetric analysis (TGA-DTA) analysis. Besides, the presence of oxidized iron oxide was confirmed from the FESEM image, which may prove the non-total iron inclusion in the host lattice as deduced from the XRD pattern analysis. The photoluminescence (PL) and diffuse reflectance ultraviolet-visible (DRS-UV-vis) analyses revealed that doping improved the visible optoelectrical properties of ZnO. The catalysis on methylene blue and 4-nitrophenol showed great potential for the ICZ-Cs over single ZnO as a result of their improved optoelectric properties.

1.2. Statement of problem

The ability to access clean water is essential for human survival. Wastewater treatment is a crucial step in reducing environmental concerns and toxins. Additionally, because of global population growth and economic development, wastewater recycling and reuse are mandatory to providing the water needed for irrigation, industry, and domestic purposes. There is a lot of interest in the development of industry and agriculture in Ethiopia. As a consequence of this development harmful wastes exposed to water bodies and Ethiopia's waste management system is poor to trigger this issues. Among those adverse contaminants, methylene blue dye and the organic pollutant 4-nitrophenol are the major one. Water treatment techniques can be divided into three categories: biological, chemical, and physical. Microorganisms are used in biological water treatments to biodegrade the contaminants in the water (Hedaoo et al., 2012). However, the efficiency of biological treatment is poor due to dyes' non-biodegradability. As a result, the biodegradation will take a long time to complete. Physical wastewater treatment techniques entail physically capturing and separating the pollutant from the water. Widely used physical adsorption technique is carbon adsorption. Even though the water is dye-free following the treatment operations, the contaminants are still present and do not removed because of the treatments' non-destructive character. In the end, this will lead to secondary contamination, which is undesirable. Other restrictions are the high cost and the need for carbon adsorption for the disposal of used carbon (Zangeneh et al., 2015).

On the other hand, chemical water treatments primarily focus on the interactions between the chosen chemicals and the pollutant that has been contaminated by chemical disinfection. Ozonation and chlorination are two examples of such treatments. However, there are drawbacks to the processes, such as the production of potentially dangerous chlorinated byproducts and the toxicity and instability of ozone (Carlos et al., 2020).

One of the most efficient and low-cost ways to achieve this goal is through photocatalytic degradation of organic dyes and contaminants. Photocatalysis is a promising approach for removing hazardous organic pollutants from industrial wastewater, and it has the potential to tackle some of the biggest environmental challenges caused by contaminated water (Kuriakose et al., 2015). Methylene blue can be degraded more effectively through photocatalysis, although some of the photocatalysts used have a number of drawbacks, such as recombination of the photogenerated electrons and electron holes, which slows down the rate of degradation (Saggioro et al., 2011). This issue will be addressed by using auto-combustion high temperature synthesis (AHS) approach to create (ICZ-Cs) Fe and Cu co-doped ZnO nanocomposite materials. This research would attempt to find solution for problems such as band gap widening and electron hole recombination by using iron and copper doping.

1.3. Objectives of the study

1.3.1. General objective

- The general objective of this study is to synthesize Fe and Cu co-doped ZnO nanocomposite (ICZ-Cs) for catalytic activity of methylene blue (MB) and 4-nitrophenol (4-NP) dyes from aqueous solution.

1.3.2. Specific objectives

- To synthesize ZnO nanoparticles (NPs), Fe and Cu co-doped ZnO nanocomposite (ICZ-Cs).
- To characterize the synthesized ZnO NPs and ICZ-Cs using different analytical techniques.
- To study the methylene blue catalytic reduction activity of the ZnO NPs and ICZ-C catalysts.

- To study the 4-nitrophenol catalytic reduction activity of the ZnO NPs and ICZ-C15 catalysts.
- To study the methylene blue dye degradation activity of the ZnO NPs and ICZ-C catalysts.

1.4.Significance and Beneficiaries

The degradation of organic contaminants that have been discharged reduces human exposure to them and the amount of oxygen that they could potentially absorb. From the perspective of human health, the issue of cancer, mutation, and skin irritability brought on by organic dyes could also be reduced. Photocatalysts with large specific surface areas, small diameters, and porous architectures that allow dyes to pass through for catalytic degradation are being researched all over the world. ZnO NPs, which have a wide band gap energy, a large exciton binding energy, improved electron mobility, and high catalytic, non-toxic, antibacterial, and biocompatible properties, are one of the most promising photocatalysts. Furthermore, it has been found that the cost of producing ZnO NPs is substantially lower than that of other nano-photocatalysts. The primary beneficiaries of this effort are the textile, paper, cosmetic, and leather processing sectors, which generate wastewater with high levels of organic dyes. The synthesis, doping and catalytic activity studies are believed to contribute much to the science which benefits the scientific community to encourage for further research activities. Additionally, these organic colors will have a lower environmental impact.

1.5. Scope of the Study

In this work, Fe and Cu co-doped ZnO nanocomposite (ICZ-C) was synthesized by a simple and facile method. The synthesized samples were characterized using XRD, TGA, FESEM-EDS, PL, UV-DRS, and FTIR. The catalytic reduction performance of the samples were investigated using methylene blue (MB) dye and 4-nitrophenol (4-NP) in aqueous solution. Its photocatalytic activity was also evaluated using methylene blue dye.

CHAPTER TWO

2. LITERATURE REVIEW

2.1. Water Pollution

Environmental contamination is growing daily and endangering both current and future generations of people globally. For all living things to live sustainably and with quality, water is one of the most vital natural resources. Global water consumption must rise above average due to the rapid growth of industrialization, urbanization, and population. As a result, the worldwide shortage of clean water sources is being caused by the excessively urgent need for water. Additionally, untreated contaminated water effluents from industries such as those in the textile, paper, rubber, batteries, pharmaceutical, and food processing sectors, domestic households, and agriculture are discharged directly or indirectly into natural water bodies, which continuously worsens the situation regarding the availability of fresh, clean water for people, animals, marine life, and plants. Organic (dyes, pesticides, halogenated medicines, and aromatic chemicals like polycyclic aromatic hydrocarbons) and inorganic (heavy metal ions) molecules that are difficult to breakdown and endanger natural resources are present in these contaminants (Gusain et al., 2020).

Everywhere we look, whether in man-made or natural objects, there is color, from the clothes we wear to everything in our environment. These hues had their origins in natural resources up until the nineteenth century. Insects and mollusks were the next most abundant group of these origins, followed by plants, trees, and lichen as vegetables. Only a dozen or so dyes have been practically employed across thousands of years, which is a reflection of the volatility of natural dyes. More than 7,000 colorants are available now, and in 1974, synthetic dyes sold for a staggering £1,500 million globally (Samsami et al., 2020). A dye is a natural or synthetic coloring agent that is used to dye or print textiles, papers, leather, and other materials so that the color of the dyed or printed items won't fade with use, exposure to heat, light, or other environmental factors. In most cases, aqueous solutions are used to apply the colors. The dyes can bind to suitable surfaces through physical adsorption, covalent bonds, in situ complexes with salts or metals, or mechanical retention (Kumar & Choudhury, 2018).

2.1.1. Source of dye pollutant

Due to their ability to produce color, synthetic dyes are a necessity in many important industries, including the leather, paper, and textile sectors. According to estimates, 700,000 metric tons of different colorings are produced each year, and approximately 100,000 dyes are produced for sale (Holkar et al., 2016). Once dyes have completed their intended function, the majority of them are frequently dumped carelessly into environmental water bodies. According to Fig. 1, significant industries are recognized as the main contributors to the environmental presence of dye effluents. More than half of the dye effluents currently found in the environment across the world come from the textile sector, which discharges most of them (54%) than any other business. The dyeing industry (21%) generates significant amounts of dye effluent from a variety of related operations, as do the paper and pulp (10%), tannery and paint (8%), and dye production (7%) industries (Mojsov et al., 2016). Although the precise quantity of dye effluents released into the environment by each company is unknown, it can be assumed that the amount is sufficiently large to pose a serious environmental concern.

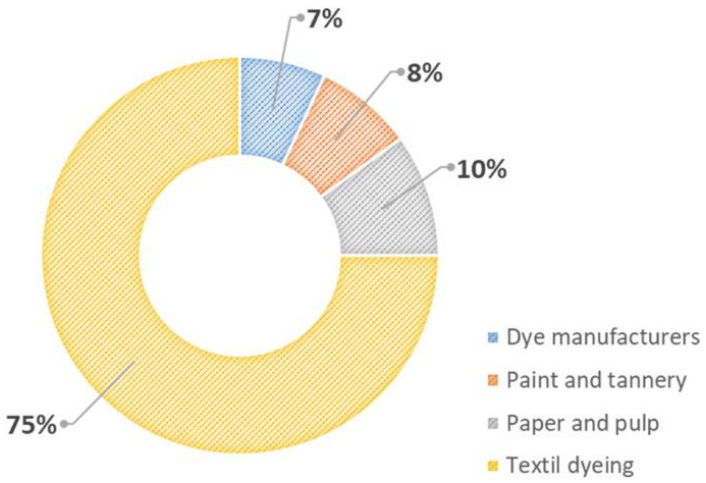

Figure 2.1. Industries that are to blame for the existence of dye effluent in the environment (Alencar et al., 2021).

2.1.2. Dyes in textile industry

Among other dye-using businesses, the textile industry is claimed to use the most dyestuff, using about 10,000 tonnes annually worldwide. In addition, this industry is noted for producing the biggest volume of dye wastewater from a single industry alone—roughly 100 tonnes of dye effluent annually. Due to the extensive use of dyes in the textile industry's

numerous processes, enormous amounts of dye wastewater are produced. Additionally, because the textile industry uses such a large amount of water, it produces many dye effluents.

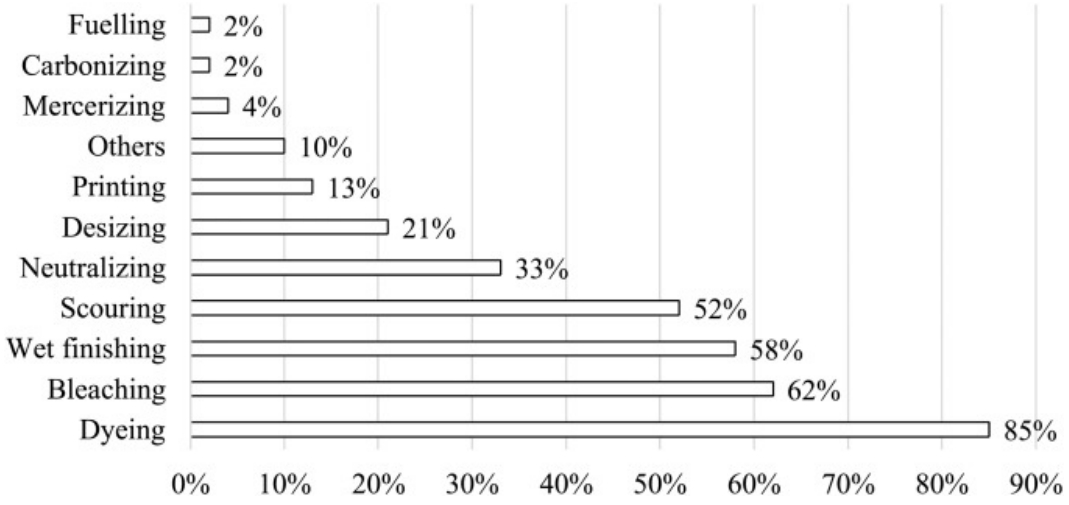

Figure 2.2. Percentage of dye mixture from each process of the textile industry (Katheresan et al., 2018)

The textile business prepares specialized combinations of chemicals, dyes, and water for a variety of operations. The residual mixture (dye effluent) is released into the environment after the process is finished. For instance, 85% of the dye used in the dyeing process is wasted. This dye effluent is the remaining dye mixture that was prepared at the start of the dyeing process (Katheresan et al., 2018). Fig. 2 displays the percentage of dye mixture expelled at the conclusion of each textile industry operation.

2.1.3. Methods of dye removal

Because there was no limit on the amount of dye that could be discharged in wastewater in the late 1990s, the only methods of dye removal used were basic water purification techniques like equalization and sedimentation (Robinson et al., 2001). Numerous studies are currently being conducted to determine the best dye removal technique so that dye wastewater can be recovered and used as needed. The biological, chemical, and physical therapies are the three groups into which existing dye removal techniques can be divided (Katheresan et al., 2018).

2.1.3.1. Biological treatment methods

In order to bio absorb or degrade the colors in the water, this includes the employment of mechanisms like aerobic and anaerobic degradation, which involve the use of suitable fungi, algae, or bacteria. Due to their extracellular nature, fungi have the benefit of being able to withstand extremely high dye concentrations. As with physical therapy approaches, these methods are also impacted by variables like pH and contact time (P. Sharma & Qanungo, 2022).

2.1.3.2. Chemical treatment methods

These include photocatalytic processes, ozonization, and the Fenton reagent approach. These procedures fall under several "advanced oxidation processes" (AOPs) (P. Sharma & Qanungo, 2022) that concentrate on completely oxidizing organic molecules to create products like carbon dioxide and water.

2.1.3.3. Physical treatment methods

Physical dye removal techniques are typically simple procedures frequently carried out via the mass transfer mechanism. Adsorption, coagulation or flocculation, ion exchange, radiation, membrane filtration, nano filtration or ultrafiltration, and reverse osmosis are common physical dye removal techniques (Katheresan et al., 2018).

2.2. Photocatalysis

In order to photo-degrade harmful chemicals in wastewater without creating any secondary waste, heterogeneous photocatalysis is used as an advanced oxidation process (AOP). Toxic chemical degradation is accomplished through photocatalysis, which is driven by semiconductor materials that operate as photocatalysts with the proper band gaps under light irradiation. The photocatalyst is a semiconductor material that produces catalytically active species upon photon absorption when exposed to light. The photon's energy ought to be on par with or greater than the photocatalyst's bandgap. The purpose of photon absorption is to create charge carriers (such as electrons and holes) that take part in redox reactions to break down hazardous chemicals that have been deposited on the surface of the photocatalyst. Because of this interaction, hydroxyl radicals (•OH) are created, which function as potent oxidants and break down hazardous compounds. The oxidation of pollutants is aided by the

positive holes that are produced. Numerous semiconductor and nanohybrid materials, including TiO_2, ZnO, SnO_2, CuO, Bi_2WO_6, WO_3, CdS, MoS_2, Ag/Ag_2Te, and g-C_3N_4, have been investigated as photocatalysts in wastewater treatment through photocatalysis. Zinc oxide (ZnO) is the most researched and employed photocatalyst due to its abundance, non-toxic behavior, economic feasibility, chemical and thermal stability, environmentally benign nature, and, most importantly, optical and electrical properties (Gusain et al., 2020). In general, photocatalysis has a number of benefits, including:

No secondary waste generation;
High degradation rate;
Reduced time cost;
Mineralization of toxic compounds;
Ambient operating conditions;
Recyclability of the photocatalyst;
Use of renewable sources, such as solar light;
Economic viability; and
Environmental friendliness.

2.2.1. Photocatalysis mechanism

In a heterogeneous photocatalysis process, the photocatalyst absorbs light with the right amount of energy when illuminated, which excites the electrons in the valence band to move into the conduction band and initiate the photochemical reaction. Following the absorption of light by a photocatalyst, four major steps occur during photocatalytic reactions: (i) formation of charge carriers over the valence band (VB) and conduction band (CB), (ii) recombination of the photogenerated electron/hole (e/h^+) pairs, (iii) trapping of the e/h^+ pairs in redox reactions, and finally (iv) the main photocatalytic reactions such as pollutant degradation (Fig. 3). The incidence of light with the same or higher energy than the energy gap (Eg) of the used semiconductor drives electrons from the VB to the CB, leaving positive holes in the VB and thus creating e/h^+ pairs in the first step. Nonetheless, the photoinduced e/h^+ combinations are not energetically stable, and some of them recombinate, neutralizing each other and emitting heat. The second stage, whether on the surface or in the bulk, significantly lowers the effectiveness of photocatalytic reactions. In the third phase, photoinduced holes and electrons transfer to the surface of the photocatalyst and react with the adsorbed species on the surface, resulting in the creation of certain active species (e.g.,

O_2, OH) capable of launching a series of redox reactions. Finally, depending on the type of photocatalytic activity, reduction and oxidation reactions occur over the CB and VB of the photocatalyst in the last phase (Pirhashemi et al., 2018).

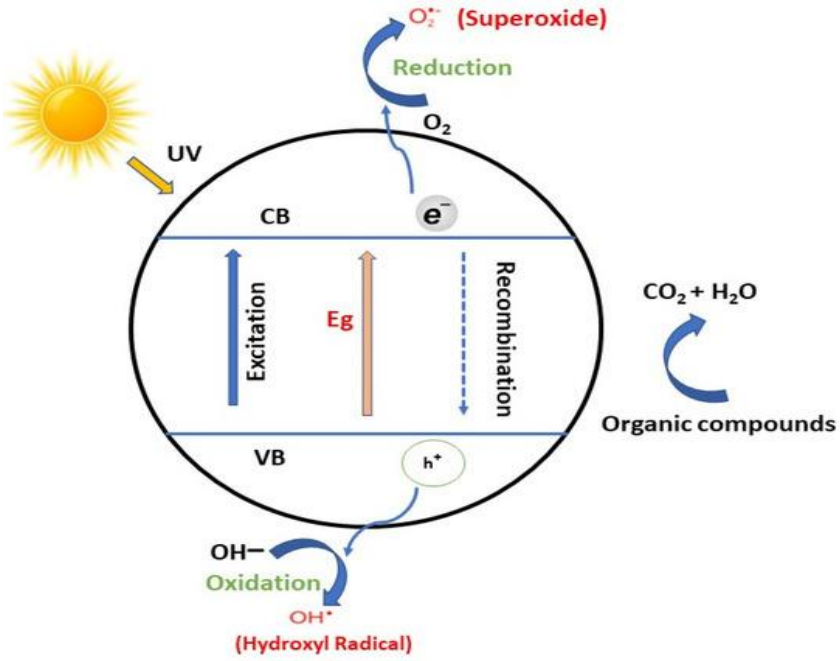

Figure 2.3. General mechanism of the photocatalysis (Gusain et al., 2020).

2.3. Factors affecting photocatalysis

Numerous factors, including pH, initial dye concentration, photocatalyst particle size and concentration, reaction temperature, light intensity, and the presence of electron acceptors, affect the photocatalytic performance of dye degradation.

The potential for an $OH^{\bullet}$ radical to form on a catalyst's surface and the reaction between dye molecules and the $OH^{\bullet}$ radical will determine how quickly dyes will photodegrade. An increase in the likelihood of the reaction between the dye molecules and the $OH^{\bullet}$ radical could be the cause of the initial increase in the degradation rate with an increase in the initial dye concentration. However, as the dye concentration rises, the catalyst's activity declines. This may be because more dye molecules are adsorbed on the catalyst surface at high dye concentrations, inhibiting the interaction between the dye molecules and the $OH^{\bullet}$ radical and decreasing the amount of $OH^{\bullet}$ radical formed (Anju Chanu et al., 2019).

Pollutants' rate of photodegradation is substantially influenced by the reaction medium's pH. The pH of the solution affects the adsorption of the pollutant, the oxidation potential of the photocatalyst's valence band, the degree of ionization, the agglomeration, and the surface charge. It is difficult to explain how pH affects the photodegradation efficiency of a catalyst because three different processes primarily influence photodegradation: (a) oxidation of pollutants due to the high oxidation potential of positive holes; (b) hydroxyl radical (•OH) attack; and (c) reduction of pollutants by the conduction band electrons. A negative charge is induced on the surface of the photocatalyst when the pH of the solution is increased beyond the isoelectronic point of the catalyst. As a result, negatively charged photocatalysts electrostatically pull cationic pollutants from the aqueous solution to adsorb, which directly influences the rate of electron transfer between the pollutant and photocatalyst for photodegradation. However, at lower pH levels (below the photocatalyst's zero point charge), the functional groups on the catalyst become protonated and cause a positive charge to be induced on the surface, which attracts anionic contaminants (Gusain et al., 2020).

The amount of catalyst can have a significant effect on photocatalysis, which is a process that involves the use of a catalyst to increase the rate of a photochemical reaction. In general, increasing the amount of catalyst can increase the rate of the reaction, up to a certain point where further increases in catalyst amount do not provide any additional benefits. This is because the active sites on the catalyst surface become saturated with reactants, and adding more catalyst does not increase the number of active sites (Gusain et al., 2020).

2.4. Metal Oxide Catalysts

Various catalytic processes have employed transition metals and their oxides. They demonstrate a variety of unique qualities and industrial uses. They can also act as sensors, ceramics, photoactive materials, superconducting materials, crystalline lasers, photoactive materials, and photosensitizers. Metal oxides have been extensively used in the fields of physical, chemical, and materials sciences. The versatile and simple-to-synthesize metal oxides have many uses. In addition, the generation, storage, and conversion of energy have all been proposed as potential uses for metal oxides. Due to their crystalline structure, morphology, doping, inherent flaws, and composition, they have advanced and distinctive functional properties. Typically, positive hole-electron pairs are formed when wide-bandgap metal oxide nanoparticles are exposed to light radiation; substrates may adsorb on the

surface of the photocatalyst and react either directly or indirectly with the produced holes and electrons (Joshi et al., 2022).

2.4.1. ZnO as a Photocatalysis

Because of its diverse properties and applications, ZnO is a well-studied photocatalyst with semiconducting properties. ZnO is an n-type II-IV semiconductor with a band gap of 3.37 eV, a high excitation binding energy of 60 meV, and good visual transmission. ZnO has several advantages, including low cost, environmental safety, high initial activity rates, and a large number of active sites with high surface reactivity. Because of its large band gap of 3.37 eV (wavelength = 380 nm), ZnO absorbs primarily in the ultraviolet. Because UV emits just 4–5% of the solar spectrum, photocatalytic applications require efficient use of solar energy. ZnO offers a number of attractive features, including non-toxicity, biocompatibility, high stability, outstanding transparency, strong room-temperature luminescence, high electron mobility, and high photocatalytic activity. Solar cells, laser diodes, thin-film transistors, UV lasers, optoelectronics, gas sensors, transparent conductive contacts, light emitter diodes, surface acoustic wave devices, and piezoelectric devices all use ZnO nanoparticles in some way. ZnO nanoparticles have been employed in a variety of applications, such as electronics, optics, cosmetics, and photocatalytic destruction of organic contaminants in water. When compared to other metal oxides, ZnO has a high degree of lattice defects on its surface area, making it an efficient photocatalyst material. Phase purity, crystallite size, surface area, dopant type, and synthesis procedures are all key factors in determining ZnO NP photocatalytic activity (Sanakousar et al., 2022).

2.4.1.1. Fundamental Properties of ZnO

Zinc oxide is a semiconductor in-group II-VI with a valence boundary between ionic and covalent semiconductors. A broad energy band (3.37 eV), high bond energy (60 meV) and high thermal and mechanical stability at room temperature make it attractive for potential use in electronics, optoelectronics and laser technology (Bacaksiz et al., 2008; J. Wang et al., 2005). ZnO is used as a sensor, energy generator, converter and photocatalyst in hydrogen production due to its piezo- and pyroelectric properties (Kolodziejczak-Radzimska & Jesionowski, 2014). As a result of its hardness, rigidity and piezoelectric constant it is an important material in ceramic industries, although its low toxicity, biocompatibility and biodegradability make it a material of interest for biomedicine and in

pro-ecological systems (Ludi & Niederberger, 2013). Considering these advantages, recent review article has described progress in the growth and applications of various ZnO nanostructures with different morphologies. The crystal structures and electronic properties of ZnO nanostructures, which undergo changes during the ZnO doping process (Dutta et al., 2009).

2.4.1.2. Crystal structure

Tetrahedral bonding is present in ZnO, and it is on the cusp of covalent and ionic semiconductors in terms of its significant ionicity. Because of this, ZnO has a large bandgap energy. ZnO can crystallize in three different ways: as hexagonal wurtzite, cubic zinc blende, and rock salt, as shown in Fig. 4 (Espitia et al., 2012). Under normal conditions, hexagonal wurtzite of ZnO is the most thermodynamically stable material. By growing ZnO on cubic substrates, however, cubic zinc blende can be stabilized. Only at comparatively high pressures would ZnO occur in the rock-salt framework (Özgür et al., 2018).

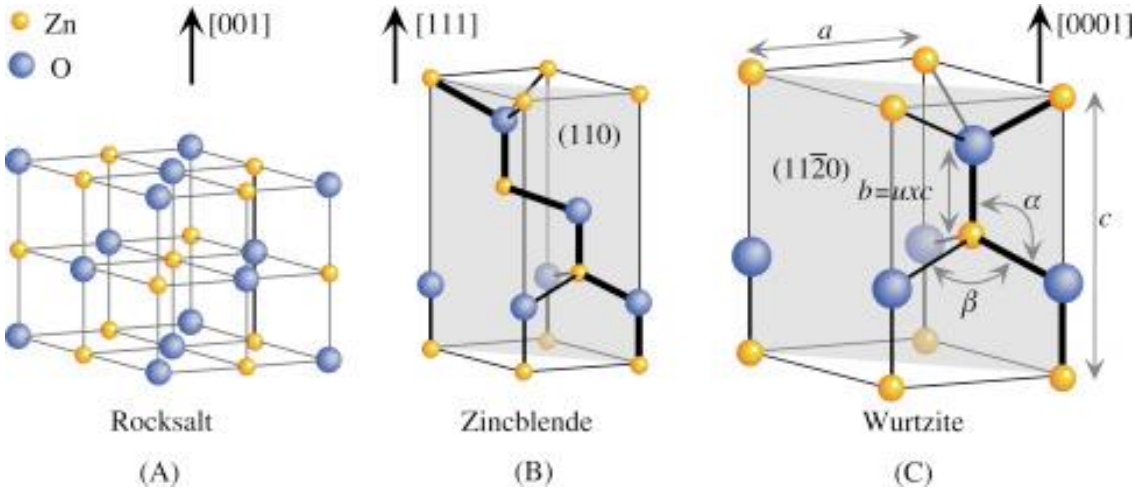

Figure 2.4. Stick and ball representation of ZnO crystal structures (Özgür et al., 2018).

2.4.1.3. Improvement of ZnO as Photocatalysis

Low quantum yield and a high photogenerated electron-hole pair recombination rate limit ZnO's photocatalytic activity. Because of this recombination process, the quantum yield is decreased and energy is lost. The electron-hole recombination route should be minimized to allow for efficient photocatalysis. The recombination problem may be resolved by metal and non-metal doping by enlarging the charge gap between electrons and holes. Additionally, dopants might capture electrons, reducing the likelihood of electron-hole

recombination, which would render the photocatalytic system inactive. Doping accelerated the photocatalytic degradation of dyes, with doped-ZnO degrading pollutants faster than undoped ZnO due to changes in bandgap energy and surface area. A larger surface area indicates a strong redox reaction; it produces more electrons and holes, boosting the band gap; the particle size reduces, which energetically participates in or correlates with the photocatalytic reaction; and the whole process has a higher degradation rate. As a result, doping is a straightforward and effective procedure (Sanakousar et al., 2022).

2.5. Doping

Doping means the introduction of impurities into a semiconductor crystal to the defined modification of conductivity. It is the addition of small quantities of an element or an impurity to pure semiconductor to change its electrical conductivity characteristics. In semiconductor doping there are two types of dopant, n-type ("n" for negative), and p-type ("p" for positive) dopants. The n-type dopants act as electron donors and have extra valence electrons with energies very close to the conduction band. When incorporated into the atomic lattice of a semiconductor, the valence electrons of n-type dopants can be easily excited to the conduction band. P-type dopants assist in conduction by accepting electrons. When a p-type dopant is incorporated into the atomic lattice of a semiconductor, it is able to host electrons from the conduction band, allowing the easy formation of positive holes (Buonsanti & Milliron, 2013).

2.5.1. Copper doped ZnO

The most effective way to raise ZnO's photocatalytic performance is by using Cu. The electrical, optical, and magnetic characteristics of ZnO are substantially altered by Cu doping. By causing lattice defects in ZnO due to Cu doping, optical absorption in the visible region is increased, which improves photocatalytic activity (Kuriakose et al., 2015). There have been some published investigations on Cu-doped ZnO nanostructures. Cu-ZnO NPs were synthesized by Min et al. (2011) using a sol-gel technique and their optical and photocatalytic characteristics were examined (Fu et al., 2011). Cu-ZnO NPs were synthesized by Mittal et al. (2014) using a co-precipitation technique, and their UV-visible light-driven photocatalytic efficiency was investigated (Mittal et al., 2014). Kurioskar et al. (2015) created Cu-ZnO NPs using a straightforward chemical process, and their structural, optical, and photocatalytic behavior was investigated (Kuriakose et al., 2015). By using a

simple wet chemical process, Yang et al. (2018) created Cu-ZnO nanostructures and discovered that they had higher photocatalytic activity than ZnO that had not been doped. Ma and coworkers illustrated the photocatalytic organic dye degradation mechanism by Cu doped ZnO catalyst (Fig. 5).

$$ZnO + h\nu \rightarrow e^{-}(CB) + h^{+}(VB)$$
$$e^{-} + Cu^{2+} \rightarrow Cu^{+}$$
$$h^{+} + OH^{-} \rightarrow \cdot OH$$
$$\cdot OH + \text{Organic dye} \rightarrow CO_2 + H_2O$$

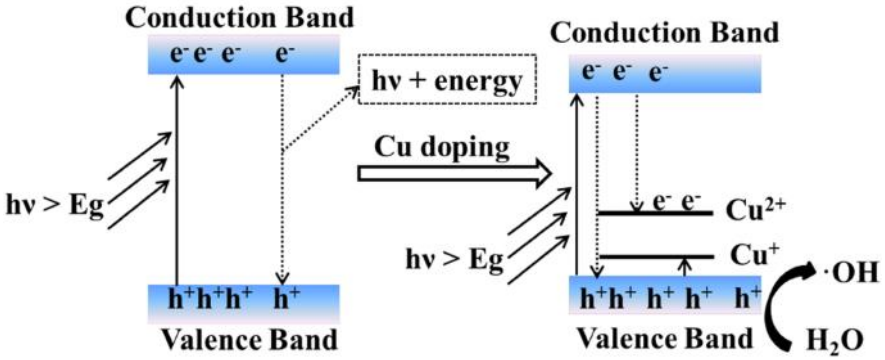

Figure 2.5. Photocatalytic mechanism of Cu doped ZnO hierarchical nanostructures (Ma et al., 2019).

2.5.2. Iron doped ZnO

Fe doping has been utilized to enhance the optical and electrical properties of ZnO material. To provide two additional free electrons to the electrical conduction, the Fe ion can actually be simply substituted on the Zn site. Thus, researchers describe the synthesis of ZnO nanostructures utilizing a polymeric complex approach that makes use of accessible metal nitrate precursors and starch as a complexing agent. For examining a material's electrical characteristics, impedance spectroscopy (IS) is regarded as a potent instrument. Different electrode contributions, grain borders, and individual grains can be identified by varying the system's applied frequency (Ma et al., 2019). As a result, the impact of Fe addition on ZnO nanomaterial's electrical, dielectric, optical, and photocatalytic properties was also examined.

(Yi et al., 2014) reported that ZnO and Fe-doped ZnO in the range of 0-2% nanoflowers were made using a basic hydrothermal process. The photocatalytic activity of the catalyst was evaluated by observing how rhodamine B (Rh B) degraded in an aqueous solution when exposed to UV and visible light (> 420 nm). Iron might be able to substitute Zn^{2+} in the ZnO

lattice in part because of its multivalent nature (Fe^{3+}/Fe^{2+}). All of the Fe-doped ZnO samples demonstrated faster photodegradation of RhB in contrast to undoped ZnO. The deterioration rates were 67, 74, 94, and 84%, respectively, in the presence of 0, 0.5, 1, and 2% Fe for 180 minutes under visible light.

2.6. Synthesis of Nanomaterials

There are two main approaches for the synthesis of nanomaterials: top-down approaches and bottom-up approaches. The term "top-down" refers to reduction by attrition and different conventional methods of comminution, which are the traditional methods of producing fine particles. In recent years, "bottom-up" production approaches have become more and more popular. The term "bottom-up approach" describes the process of either building a substance from the bottom up, atom by atom, molecule by molecule, or cluster-by-cluster (Tulinski & Jurczyk, 2017). Top-down approaches have a number of significant drawbacks, including the inability to regulate the size, morphology, and other structural characteristics of the created particles. The form, size, and morphology of the resulting particles can be significantly controlled using bottom-up approaches, which begin at the molecular level. Because the structural properties of the resulting products are delicately controlled, bottom-up techniques are more common and widely used. Reagents include growth inhibitors, ligands, and surfactants that can help control the growth process of nanostructures in the bottom-up approach (Siddique & Gonzalez-cortes, 2022). Top-down approaches include mechanical milling, laser ablation, sputtering, and electro-explosion. While bottom-up approaches include Chemical Vapour Deposition, green synthesis, sol-gel, co-precipitation, solution combustion etc. Fig. 6 displays the different top-down and bottom-up approaches.

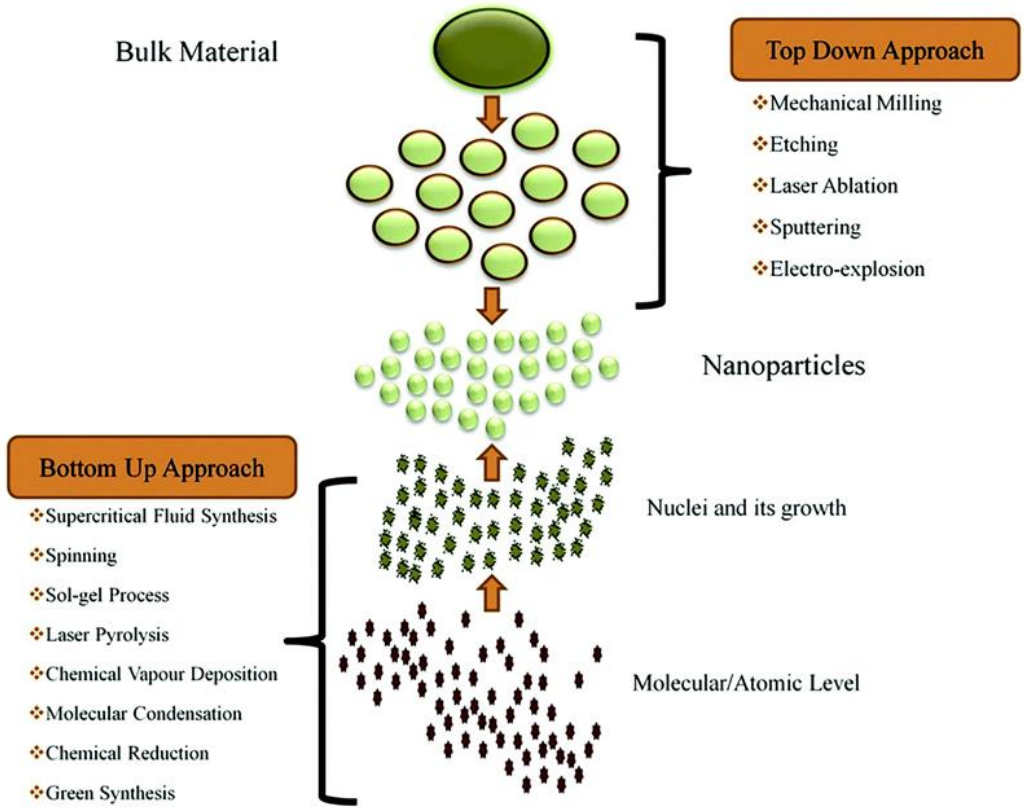

Figure 2.6. Top-down and bottom-up methods for synthesizing nanomaterials (Baig et al., 2021).

2.6.1. Fundamentals of the Bottom-up Synthesis Approach

Due to the essential differences between the bulk equivalents and the nanoscale-sized materials, attention has been generated in numerous disciplines. The current development is the bottom-up synthesis of nanocrystals with precise shape, size, and structure by comprehending the precursor breakdown, nucleation, and growth processes under challenging external and interior conditions. Controlling the nucleation and growth development processes are crucial procedures before the formation of nanocrystals. The first model to explain precursor decomposition and reduction, nucleation, development into seeds, and finally growth into nanocrystals in solution was LaMer's group theory (Abebe et al., 2022). In the 1950s, LaMer and his colleagues proposed the idea of burst nucleation, transferring the concept of critical nucleation theory (CNT) to NP syntheses. Their investigation into diverse oil aerosols and sulfur hydrosols led to the development of the ground-breaking idea. In the burst nucleation process, homogeneous nucleation causes the simultaneous generation of many nuclei, which then expand without further nucleation. That concept of nanoparticle (NP) formation's fundamental principle is the distinction between

nucleation and growth. One interpretation is that a homogeneous phase and a heterogeneous phase are separated. The particle size distribution during growth can be managed using such a procedure. The following is the mechanism, which is shown in Fig. 7: (I) The concentration of monomers is rising (in the case of metallic NPs, most likely due to reduction) and reaches, at a certain time, a certain critical supersaturation level (CS), at which homogeneous nucleation is possible but "effectively infinite"; (II) The saturation is rising and reaches a level (Cmin) at which the energy barrier (activation energy) for nucleation can be overcome, leading to rapid self-nucleation. At the self-nucleation stage (II), the predicted corresponding particle concentration with respect to time would increase quickly, and at the final growth stage (III), it would remain roughly constant (Polte, 2015).

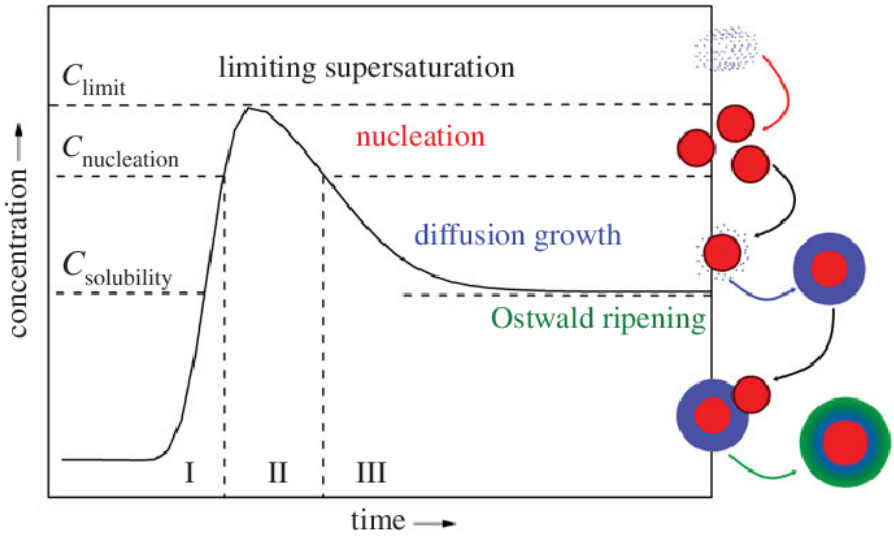

Figure 2.7. The LaMer model of nucleation and growth (Dunne et al., 2015).

2.6.2. Capping Agent

Currently, the term "capping agent" refers to both surfactants and ligands in general. Capping agents bind to the surface of the particle and are essential in the production, processing, and application of nanomaterials. The bond saturation generated by the capping agents on the nanoparticle's surface protects the particle from its surroundings. This makes it possible to control the synthesis's nucleation and growth kinetics. Surface capping agents reduce the surface energy of growing nanoparticles by selectively attaching to specific features. The capping agents may also restrict the transport of additional chemicals to the nanoparticle surface. They bonded to the nanoparticle surface, inhibiting aggregation and controlling particle growth throughout synthesis (Rafeeq et al., 2022). Polymers are utilized as both stabilizing and reducing agents in the production of nanomaterials. Furthermore,

they operate as a structural guiding agent, assisting in tuning the structure of materials towards a given shape.

In addition to producing particles with an extremely narrow size distribution, polymer-stabilizing chemicals can prevent nanoparticles (NPs) from clumping together unintentionally. Not less significant is the fact that the stabilizing agent stops metal atoms from depositing on the surface of metallic NPs by forming stable, resilient, and multifunctional shells that protect the core's features (Dzhardimalieva & Uflyand, 2018). A popular polymer used as a stabilizing and reducing agent is polyvinylpyridine (PVP). PVP is a non-toxic, water-soluble polymer with a significant quantity of a carbonyl group that interacts adhesively with NPs at room temperature. As a result, once the polymer caps the NPs, the surface energy-driven aggregation is reduced. Adsorption of surfactants onto the surface of the nanocrystals stabilizes them. In order to prevent aggregation or agglomeration, the density of the surfactants increases with decreasing entropy (increasing Gibbs free energy) as the distance between the nanocrystals decreases (Abebe et al., 2022).

2.6.3. Sol-gel auto- Combustion Synthesis Approach

The sol-gel auto-combustion method is one of the developing synthesis procedures as a viable replacement for the production of nanoparticles as compared to other methods (Pathak et al., 2016). The auto-combustion process is self-sustaining; once the reaction has started, a high temperature is generated due to the reaction's exothermic properties, ensuring the synthesis and crystallization of metal oxides in a timely manner. This approach frequently prevents the instantaneous creation of particles from aggregating (Novitskaya et al., 2021).

The sol-gel auto-combustion process, which uses a low reaction temperature (80–100 °C) and a quick turn-around for powder synthesis, is one of the most practical and efficient wet chemical procedures (Sivakumar et al., 2011). A one-step procedure results in a large amount of fluffy and fine powder. It is based on the creation of sol, followed by gelation and combustion in a heated solution containing the needed metals' salts combined with the right fuel. Fig. 8 shows schematics of synthesis of ZnO nanoparticles by the sol gel auto-combustion approach. The efficiency and creation of high-quality fine powder (nanometer dimension) depends on the preparation environment and preparative factors including fuel type, fuel/metal nitrate ratio, pH, and annealing temperature (Bhagwat et al., 2019).

Additionally, the heat produced during combustion (enthalpy) and the flame temperature produced during auto combustion are the main factors influencing the parameters of the resulting powder, such as phase purity, particle size, surface area, and agglomeration (Bhagwat et al., 2019; Chauhan et al., 2016). These variables are all influenced by the fuel's composition. The choice of an appropriate fuel becomes crucial for producing the desired qualities in the finished product since the fuels differ in their capacity for complexing, reducing, and the amount of evolved gas they contain.

Citric acid ($C_6H_8O_7$), dextrose ($C_6H_{12}O_6$), sucrose ($C_{12}H_{22}O_{11}$), urea (CH_4N_2O), glycine ($C_2H_5NO_2$), and other organic chemicals are frequently utilized as fuels in sol-gel auto combustion synthesis. Urea, glycine, and citric acid are thought to form potent complexes with the metal cations in the solution. These fuels do two things: they produce CO_2, H_2O, and heat in an exothermic process during combustion; and they create complexes with metal ions to make homogenous mixing of the cations in solution easier. It is believed that nitrogen is liberated as a gaseous component; enhancing the porosity of the produced materials, as nitrogen, itself does not participate in the redox reaction. The type of fuel has an impact on the intensity of the combustion reaction as well (Lazarova et al., 2017). Sol-gel auto-combustion has several benefits, including good chemical homogeneity, high purity and crystallinity, fine particle size distribution, straightforward setup procedures, straightforward equipment, quick processing times, and minimal external energy consumption to start the process (Costa et al., 2007; Zaid et al., 2017).

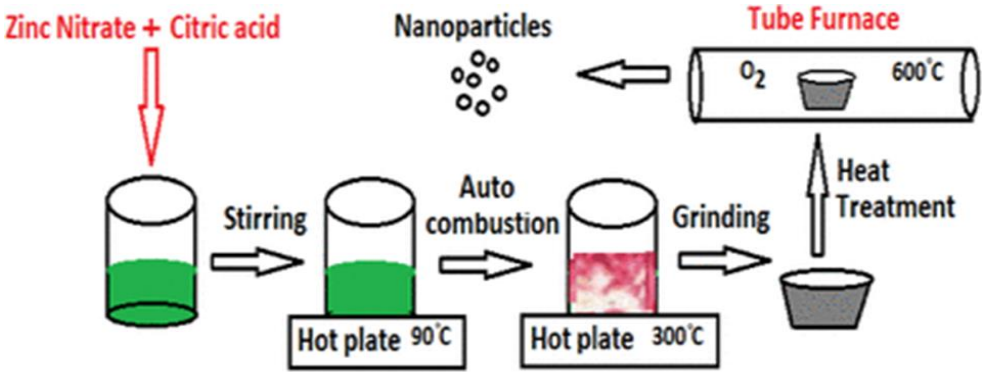

Figure 2.8. Sol gel auto-combustion synthesis of ZnO nanoparticles (Soleimani et al., 2018).

CHAPTER THREE

3. MATERIALS AND METHODS

3.1. Chemicals and Reagents

The chemicals and reagents were analytical grade and used without further purification. Zinc nitrate hexahydrate (Zn $(NO_3)_2$. $6H_2O$ (Sigma Aldrich, 99%), Copper nitrate trihydrate (Cu $(NO_3)_2$. $3H_2O$ (Sigma Aldrich, 99%), iron nitrate nonahydrate (Fe $(NO_3)_3$. $9H_2O$ (Sigma Aldrich, 98%), Poly (vinyl alcohol) (PVA, Thermo Fisher Scientific India Pvt. Ltd.), methylene blue ($C_{16}H_{18}ClN_3S$) (Sigma Aldrich) were used, distilled water was used throughout the experiment.

3.2. Synthesis of ZnO NPs and ICZ-Cs

With some modifications, such as using the PVA polymer as a reducing and capping agent, ZnO NPs and ICZ-Cs were synthesized using the auto-combustion high-temperature synthesis approach as reported in the Gao et al. study (Gao et al., 2016). The detailed steps involve first dissolving 1 g of the PVA polymer in 50 mL of distilled water while stirring with a magnetic stirrer at about 75 °C for nearly 15 min. Then, in this cooled PVA solution, approximately 0.25 molar of zinc nitrate salt was mixed for just over half an hour of stirring. The gel produced at the stage of water dehydration, at about 85–120 °C, was further heated to the polymer–surfactant ignition temperature range of 150–210 °C (the temperature at which combustion and self-propagation begin). Finally, the combusted, visually porous material is gently crushed to reduce its size, calcined at 500 °C for 3 hours, and then used for further characterization and application. The ICZ-Cs were also synthesized dissolving 1 g of the PVA polymer in 50 mL of distilled water while stirring with a magnetic stirrer at about 75 °C for nearly 15 min. After that in this cooled PVA solution 1%, 5%, 10%, and 15% of Fe and Cu nitrate salt with 99%, 95%, 90%, and 85% of zinc nitrate salt was mixed in different beaker for just over half an hour of stirring to form 0.25 molar each solution concentrations. The formed gel was heated at about 150-210 °C. Finally, the combusted material was crushed, calcined at 500 °C for 3 hours, and then used for further analysis and purpose. The ICZ-Cs1, ICZ-Cs5, ICZ-Cs10, and ICZ-Cs15 represent 1%, 5%, 10%, and 15% dopant concentrations, respectively. Schematic of the preparation of ICZ-Cs is presented in Fig.9 (B. Liu et al., 2016).

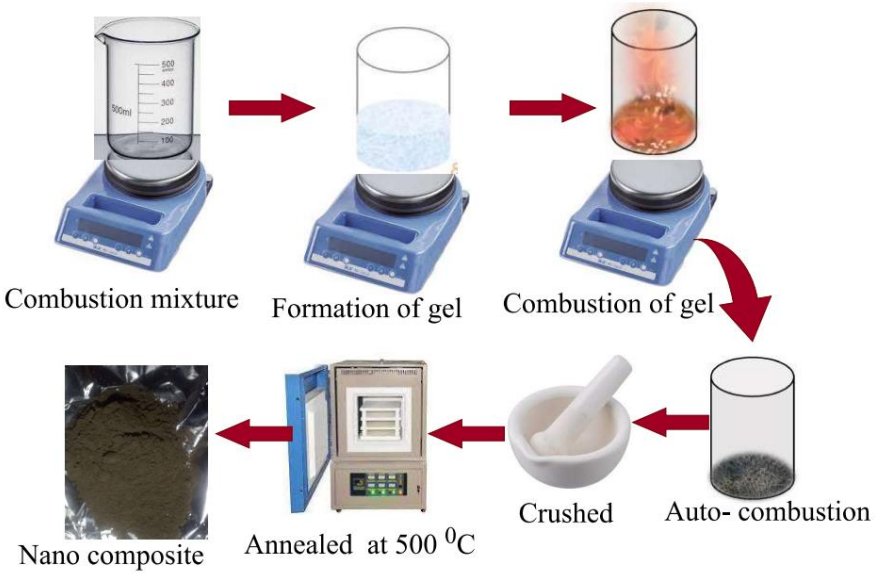

Figure 3.1. Schematic representation on preparation of ICZ-Cs.

3.3. Methylene Blue Catalytic Reduction.

The methylene blue clock catalytic redox reaction involves the transformation of methylene blue (MB) into leuco-methylene blue (LMB) in the presence of a catalyst and $NaBH_4$, which is then oxidized back into MB by adding NaOH. For this reaction process, 45 mg of $NaBH_4$ was added to 15 ppm (30 mL) of MB solution. Then, 10 mg of each catalyst (NPs and ICZ-Cs) was added to the MB-ion solution. The UV-vis spectrophotometer was used to control the reduction process runs from 200-800 nm within 1 minute time interval. A 0.01-M solution of NaOH was added to run the LMB-to-MB clock reaction (Naseer et al., 2022).

3.4. 4-Nitrophenol Catalytic Reduction

A recent study was also used as a reference to conduct the 4-NP to 4-AP reduction processes with slight experimental conditions and concentration changes (Naseer et al., 2022). Here, 45 mg of $NaBH_4$ was added to 30 mL of 4 NP solution (15 ppm), which has a yellow colour. After that, the mixture was mixed with 10 mg of each NPs and ICZ-Cs catalyst. The UV-vis spectrophotometer was used here also to monitor the catalytic reduction process that runs from 200-800 nm within 1 minute time interval.

3.5. Photocatalytic Activity

According to the method report with modification (Abebe et al., 2021), the degradation of MB dye was used to test the photocatalytic activities of the synthesised samples. All of the tests were conducted in an open environment at ambient temperature. To verify the catalyst-pollutant adsorption-desorption equilibrium in each experiment, 20 mg of metal oxide catalyst was introduced to 100 mL of MB solution (10 mg/L), followed by stirring for 30 minutes in the dark. The mixture was consistently mixed during the tests. The light was turned on, and a 150 W halogen lamp was used as the visible light source after 30 minutes of stirring in the dark. To separate the photocatalyst particles, 8 mL of the slurry was taken at predefined irradiation periods and centrifuged (3000 rpm, 20 min). The degradation efficiency in % was computed using Equation 1, and the MB concentration was determined using a UV-visible spectrophotometer (UV-3600Plus series) measuring the absorption maximum at λ max = 664 nm. In order to examine reaction dynamics, the pseudo-first-order kinetics equation (Equation 2) was used.

$$\text{Degradation yield } (\%) = \frac{C_0 - C_t}{C_0}\ x\ 100 \qquad (1)$$

Pseudo 1st and 2nd order kinetics equation were utilized in the equations to determine the kinetics of photodegradation.

$$Pseudo-\ first-order\ kinetics;\quad ln\ \frac{C}{C_0} = -kt \qquad (2)$$

$$Pseudo-second-order\ kinetics;\ \frac{1}{Ct} - \frac{1}{C0} = kt \qquad (3)$$

Where C_0 is initial dye concentration (mg L^{-}), C_t is the dye concentration (mg L^{-}) at a time and k is pseudo-first-order reaction rate constant (min^{-1}).

3.6. Characterization

X-Ray Diffraction (XRD, Shimadzu-7000, Detector(s): Scintillation Counter,X-RayTube:2kW,Cu, NF Type (Opt. 2.7kW Cu, BF Type),X-Ray Generator:Max. Output 3kWGoniometer Type: Vertical Type (Rate 1000°/min), Scanning radius: 185 mm Analysis Diameter: up to 400 mm) was used to characterize the crystallinity, crystalline size, and structure of ZnO and ICZ-Cs. The thermal stability of ZnO and ICZ-C15 were investigated by using Thermal Analysis Technique (TGA-DTA; S/N: C30575100456TK; detector: DTG-60H power supply specification AC 100V, 120 V, 230V, 1500 VA, 50/60 Hz) in a nitrogen atmosphere with a flow rate of 50 mL/min. The chemical bonding analysis

of ZnO and ICZ-C15 were determined by using Fourier Transform Infrared Spectroscopy instrument FT/IR-6600typeA (S/N: A013861790), 2 mm/sec scanning speed, detector TGS Max resolution: 0.4 cm^{-1}; S/N ratio: 45,000:1). Field Emission Scanning Electron Microscope (FESEM) and Energy Dispersive analyzer (EDX) (FE-SEM, ZEISS SIGMA VP ,resolution: 1.3 nm, accelerated voltage 0.1- 30 kV) were used to examine morphology and elemental composition of both samples. The materials optical properties and energy band gap were assessed by a double beam ultraviolet-visible machine (UV-vis, P9 spectrophotometer). The optical and electron hole recombination properties before and after doping were studied by photoluminescence spectroscopy (PL, CaryEclipse fluorescence spectrophotometer S/N: MY18490002, the scan rate being 600 nm/min) with a laser excitation wavelength of 325 nm. Transmission Electron microscope (TEM) using (TEM Tecnai G2F20 at point to point resolution of 200 kV) was used for morphology and analysis. UV-vis spectrophotometer (UV-3600Plus series) was used to evaluate methylene blue and 4-nitrophenol degradation.

From XRD data the crystallite sizes were determined by Scherrers' equation,

$(K\lambda)/ (\beta\cos\theta)$ (4)

Where k is constant (which is 0.9 for spherical symmetry), λ is the x-ray radiation wavelength (which is 0.15406 nm), β is equal to the full width at half the maximum of the peak, and θ is the Bragg x-ray diffraction angle between the incident and reflected rays (D. Sharma & Jha, 2017).

The absorption spectra was calculated from reflection spectra by Kubelka-Munk function:

[2] $a/S = \frac{(1-R)2}{2R}$ (5), Where a is the absorption coefficient, S is the scattering coefficient that is practically wavelength independent when the particle size is larger than 5 μm, and R is the reflectance.

The material synthesis was carried out entirely at Adama Science and Technology University (ASTU) in applied chemistry laboratory. Photocatalytic activity, XRD, and UV-vis spectroscopy analysis was performed in ASTU material science and engineering laboratory. UV-vis- DRS, TEM, and FESEM-EDX analysis was performed in India.

CHAPTER FOUR

4. RESULTS AND DISCUSSIONS

4.1. Thermal Analysis

The thermal stabilities of the polymer-precursor composites were studied using the thermogravimetric-differential thermal analysis (TG-DTA), as shown in Fig. 4.1. Fig. 4.1 shows the ZnO-PVA decomposition behaviour, in which two small and broad decompositions below 200 ℃ and intense decompositions at about 393 and 447 ℃ were observed. At lower temperatures, the first mass losses are caused by surface and interstitially adsorbed water molecules. While the other intense stability loss in the PVA-ZnO composites is due to the side chain and main chain PVA polymer decomposition to give pure ZnO phase (Dai et al., 2018; Radhamani et al., 2016). The maximum PVA decomposition temperature (from the plotted onset decomposition result, T_{onset}) to give pure ZnO was 490 ^{o}C.

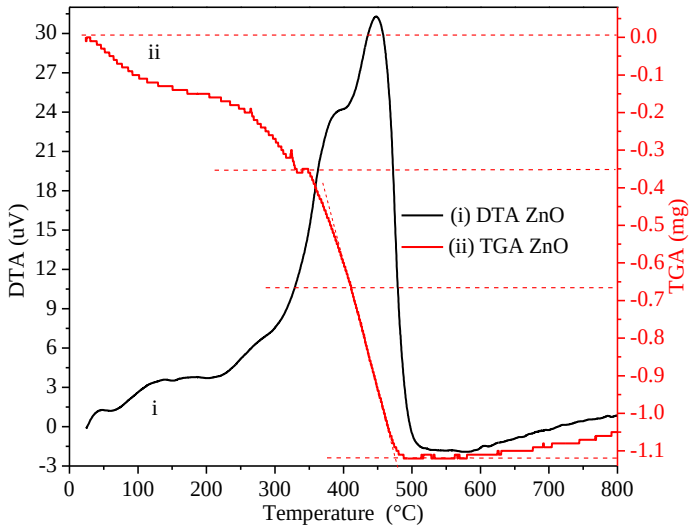

Figure 4.1. The TG-DTA thermal stability analysis: the DTA (i) and TGA (ii) plots of ZnO NPs, respectively.

4.2. Crystallinity Analysis

Herein, the pure zinc, copper, and iron oxides NPs and ICZ-Cs with different concentrations ranging from 1–15% were synthesised by the AHS synthesis approach. The ZnO NPs and ICZ-C have been calcinated at 500 °C, which is the optimum temperature selected on the TGA-DTA stability analysis. As shown in Fig.4.1, inset label i, the XRD peak angle of 19.4

degrees with a corresponding crystal plane of 101 matches with PVA; JCPDS 00-053-1847 (Selvi et al., 2019). A peak for PVA polymer was not detected on the composite's XRD pattern. The absence of PVA on the composite XRD pattern confirms its total decomposition at 500 °C. The seven major XRD peak positions (for ZnO) of 31.7, 34.4, and 36.2, 47.6, 57.5, 62.7, and 68 degrees with the respective crystal planes of (100), (002), (101), (102), (110), (103), and (112) match the hexagonal wurtzite structure with the P63mc #186-1 space group (JCPDS 00-036-1451) (Paraguay-Delgado et al., 2022). As shown in the XRD pattern results of the composites (Fig. 4.2a, inset labels ii–iv), for 1% copper doping, no visible copper oxide independent peak was detected. However, increasing the percentage from 2 to 15, the appearance of a copper oxide-independent peak was detected at about 35.4 and 38.7 degrees, which match with the CuO crystal planes of (111) and (200), respectively. (Costas et al., 2022). Besides, increasing the copper dopant percentage results in increasing the CuO crystal-independent peak intensity. The increase in intensity indicates an increase in the CuO crystal abundance in the arbitrary unit. However, no iron peak was detected on the composite's XRD pattern within the instrument detection limit, indicating its better solubility level or dominance by ZnO compared to copper (Khan et al., 2020). As the percentage of dopants increases, the ICZ-C peak intensity decreases, particularly on the 15% doped ICZ-C.

The calculated approximate crystallite sizes for ZnO and ICZ-Cs were found to be 23 nm and in the range of 26–38 nm, respectively. The reduction in crystallite size and intensity as the iron dopant percentages increased was reported to be due to the smaller sizes of iron, which prevent crystal aggregation (Samanta et al., 2020). Thus, the ICZ-C15, which has the smallest crystallite size (26 nm) compared to the other ICZ-Cs, was selected for further analysis.

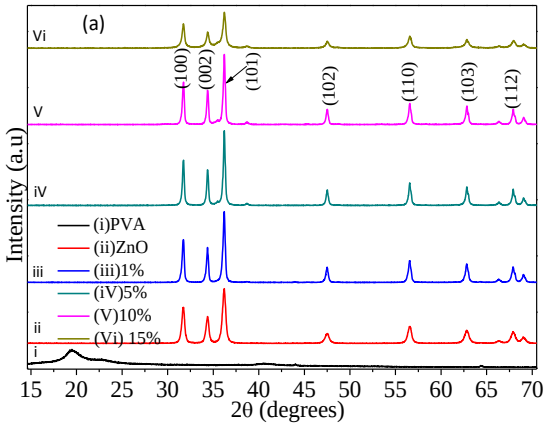

Figure 4.2. XRD patterns of the polymer, NPs, and nanocomposites: XRD patterns of PVA, ZnO, and ICZ-C1-15.

Increasing the calcination temperature and time promotes NPs aggregation (Senobari & Nezamzadeh-Ejhieh, 2020). This NPs aggregation behaviour with increasing temperature and time is due to their greater surface energy compared to the bulk (Hotze et al., 2010). Fig. 4.3 shows the XRD pattern of ICZ-C15 materials calcined at 500 °C for 30 min, 1 h, and 3 h. The obtained result shows that increasing the calcination time from 30 min to 3 h results in increased crystallisation and crystallite size from 10 nm to 26 nm. The increase in the crystallite size with increasing calcination time confirms the aggregation of the NPs with time. However, 30 min and 1-hour result showed almost similar crystallite sizes, unlike the 3-hour result, which shows an aggressive change in crystallite size. Despite having a slightly larger surface area than 30 min, the 1 hour of calcination time was chosen to maintain confidentiality on the total decomposition of the capped uncombusted and other different impurities.

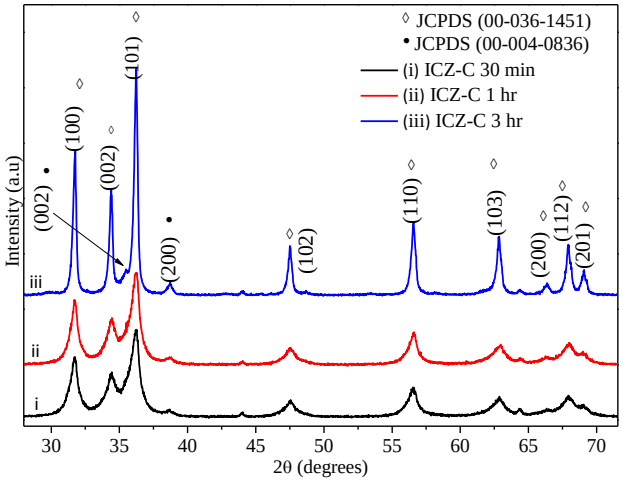

Figure 4.3. The XRD patterns of optimum ICZ-C15 calcinated at 500 °C shown at different times.

Fig. 4.4a shows the XRD pattern of polyvinyl alcohol, zinc oxide, ICZ-C, copper oxide, and iron oxide. The XRD pattern of single iron oxide that has an angle position of 24.2, 34.2, 35.7, 40.9, 49.5, 54.1, 57.6, 62.5, and 64.1 degrees with a corresponding crystal plane of (011), (104), (110), (113), (024), (116), (122), (214), and (002) confirms the hematite (α-Fe_2O_3, space group R-3c #167-1) phases of iron oxide (JCPDS 0-033-0664). The XRD pattern for copper oxide showed three phases: Cu, tenorite (CuO), and cuprite (Cu_2O). The XRD pattern angle positions of 32.5, 35.5, 36.4, 38.8, 48.9, 53.5, and 61.5 degrees with a corresponding crystal plane of (110), (002), (111), (200), (20-2), and (020) match with the CuO phase (space group: C2/c #15-1) (JCPDS 00-004-0836). The XRD pattern angle positions of 29.6, 36.4, 42.4, and 58.3 with the corresponding crystal planes of (110), (111),

(200), and (220) match with the Cu_2O phase (JCPDS 00-005-0667) (Lupan et al., 2020). The peak positions of 43.4 and 50.5 correspond to the cubic Cu metal phase (JCPDS 00-004-0836) (Uthirakumar et al., 2020), with the corresponding crystal planes of (111) and (200). The dominance of the CuO phase is probably due to the phase transformation of Cu to Cu_2O and then to CuO within a one-hour heating period at 500 °C (Choudhary et al., 2018). However, on the ICZ-C15-1 h composite, only the CuO phase at 35.5 and 38.8 degrees was detected, which is probably due to its abundance. On the composite, no hematite peak was detected, indicating its dominance by ZnO. Fig. 4.4b is the magnified view of ZnO and ICZ-C15, in which a slight high-angle peak shift was detected, which is attributed to either copper or iron inclusion in the ZnO crystal lattice. At this stage, it is not possible to understand whether there is interstitial or substitutional incorporation of copper or iron by simple XRD analysis. This requires site-specific atomic resolution imaging techniques such as scanning transmission electron (STEM) micrographs with different detectors (Gunawan et al., 2012; Rossell et al., 2012).

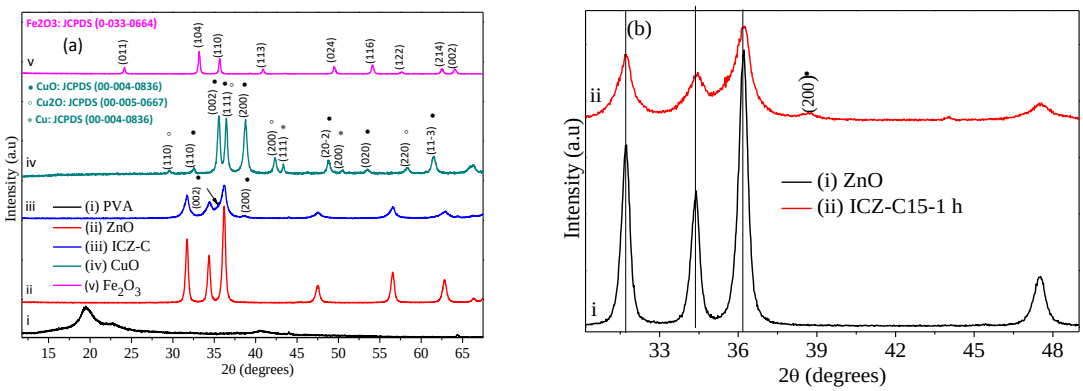

Figure 4.4. (a) The XRD patterns of PVA, CuO, Fe_2O_3, ZnO, and ICZ-C15, (b). The magnified XRD patterns of ZnO and ICZ-C15.

4.3.Morphological analysis

The morphological analysis for ZnO NPs (Fig. 4.5) and ICZ-C15 (Fig. 4.6) was performed by the FESEM-EDX technique at two different magnifications (2 µm and 300 nm). The NPs are clearly observed with good distribution on the ZnO and ICZ-C15 surfaces. Besides, the materials are highly porous, in which the porosity occurred during the evolution of the gaseous product at the precursor-PVA complex ignition temperature to give a spongy-type morphology (Abebe et al., 2022; Carlos et al., 2020). The morphologies for the ICZ-C15 seem to have a rod-type, one-dimensional morphology. As seen in previous studies (Abebe et al., 2023), the one-dimensional morphology was also not from copper, confirming it is

due to iron. Tuning the spherical morphology to one, two, or three morphologies is a crucial strategy for enhancing material applications such as sensors and catalysis (Devan et al., 2012). Fig. 4.5a and b and 4.6a and b show the FESEM images of ZnO and ICZ-C15, respectively. The EDX analysis showed the presence of oxygen and zinc at 0.5 and 1 KeV as major peaks, respectively, for ZnO NPs (Fig. 4.7). Besides, the presence of oxygen, iron, copper, and zinc as major peaks at 0.5, 0.7, 0.9, and 1 KeV, respectively, was confirmed on the ICZ-C15 surface (Fig. 4.8). The compositional analysis for both ZnO and ICZ-C materials is given as an inset in each EDX spectrum. For the ICZ-C15, the obtained compositions are perfect and agree with the ratio taken from the precursor during synthesis (Fig. 4.8). A precise dopant distribution on the surface of the host can create enormous defects, which alter crucial host material properties (Abebe & Murthy, 2022). The distribution of iron and copper dopants on the surface of the ZnO host was confirmed by the EDX elemental mapping analysis. The EDX layered image was taken from an electron image (see Fig. 4.5d and 4.6d). The mapping analysis showed the homogenous copper and iron dopant distribution on the surface of the ZnO host. The EDS elemental mapping images of zinc, oxygen, copper, and iron are given as red, green, aqua, and purple colors, respectively (see Fig. 4.5 and 4.6). The absence of any other elements and good elemental distributions indicate the potential of the AHS synthesis approach for synthesizing pure and highly distributed dopant composites.

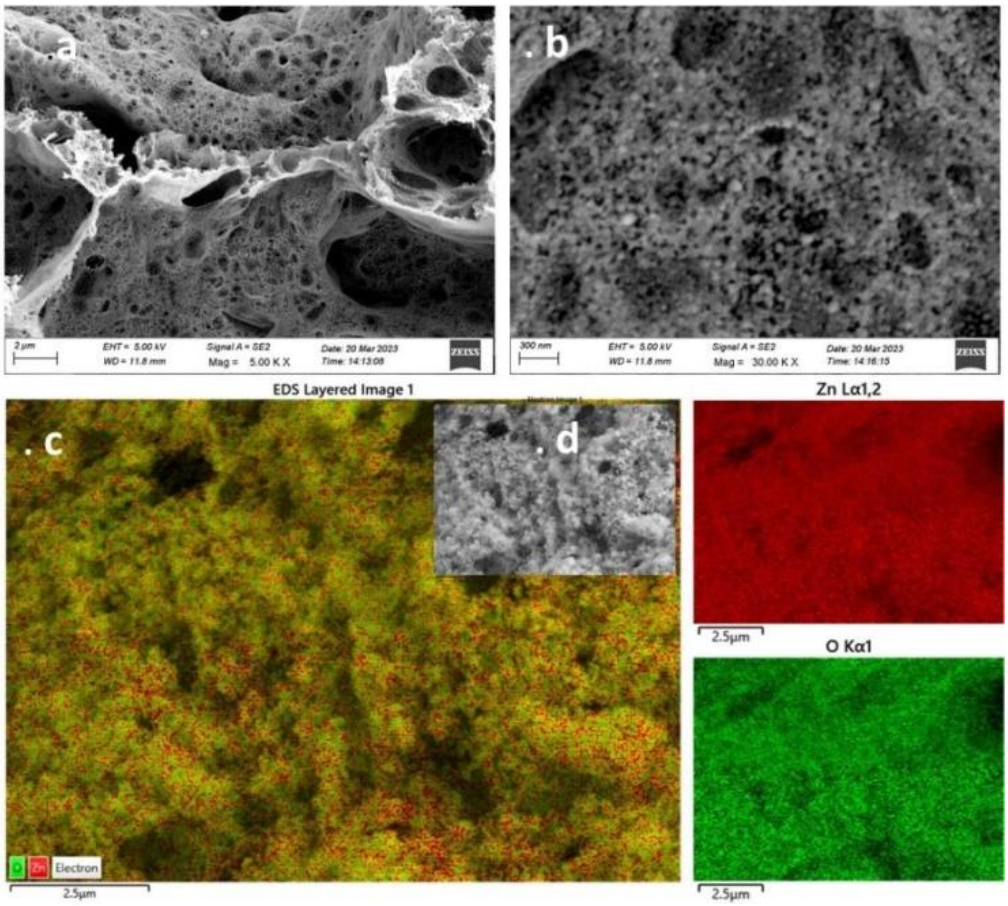

Figure 4.5. FESEM morphological and EDS elemental mapping analysis for ZnO NPs: (a) and (b) are the FESEM images for ZnO at 2 µm and 300 nm magnifications, respectively; (c) is the EDX layered image; (d) is the FESEM image from which the EDX mapping analysis was conducted.

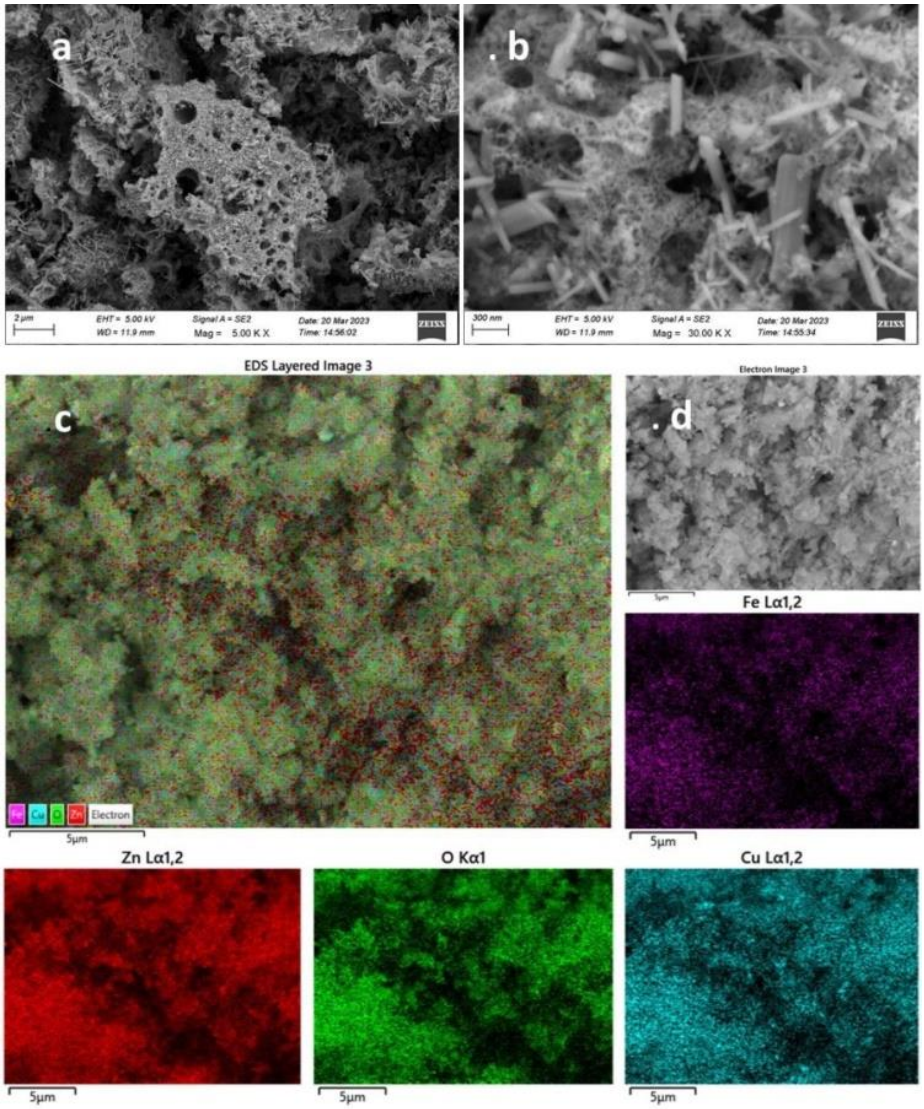

Figure 4.6. FESEM morphological and EDX elemental mapping analysis for ICZ-C15: (a) and (b) are the FESEM images for ICZ-C15 at 2 µm and 300 nm magnifications, respectively. (c) The EDX layered image; (d) the FESEM image, from which the EDX mapping analysis was conducted.

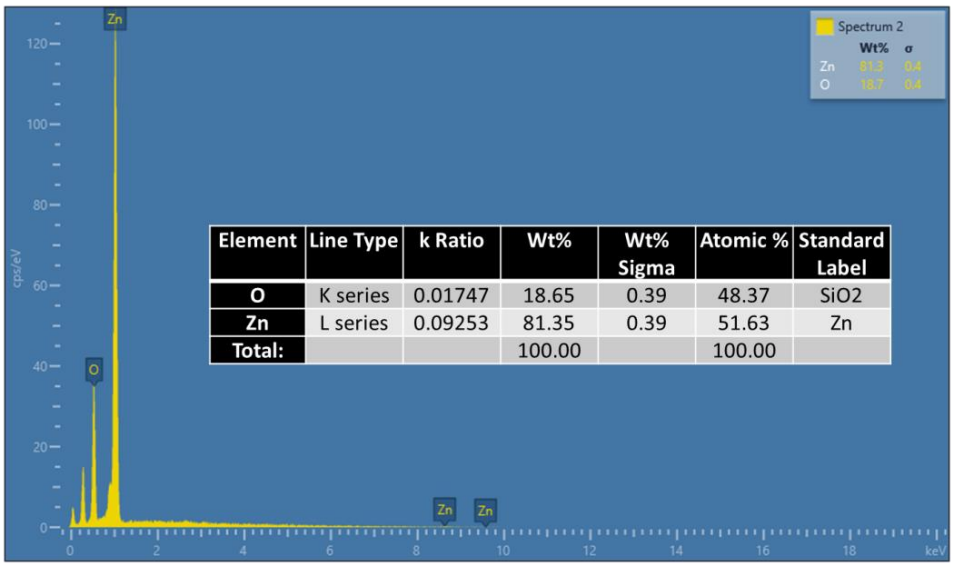

Element	Line Type	k Ratio	Wt%	Wt% Sigma	Atomic %	Standard Label
O	K series	0.01747	18.65	0.39	48.37	SiO2
Zn	L series	0.09253	81.35	0.39	51.63	Zn
Total:			100.00		100.00	

Figure 4.7. EDX compositional analysis spectra for ZnO NPs.

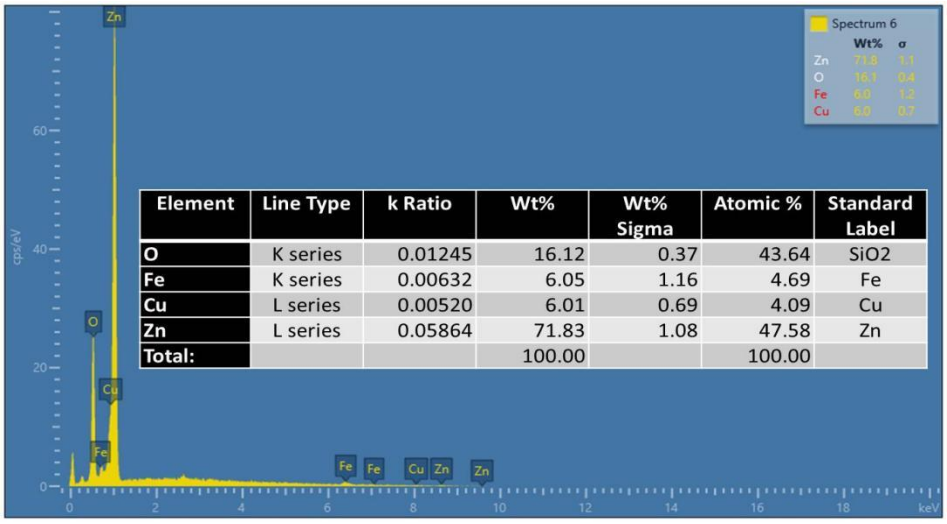

Element	Line Type	k Ratio	Wt%	Wt% Sigma	Atomic %	Standard Label
O	K series	0.01245	16.12	0.37	43.64	SiO2
Fe	K series	0.00632	6.05	1.16	4.69	Fe
Cu	L series	0.00520	6.01	0.69	4.09	Cu
Zn	L series	0.05864	71.83	1.08	47.58	Zn
Total:			100.00		100.00	

Figure 4.8 The EDX compositional analysis spectra for ICZ-C15.

4.4. Transmission Electron Microscopy (TEM) Analysis

As shown in Fig. 4.9, transmission electron microscopy, high-resolution transmission electron microscopy, and selected area electron diffraction (TEM-HRTEM-SAED) analytical techniques were used to further analyze the particle size, morphology, and crystallinity of nanoscale-sized ZnO NPs and ICZ-C15. The ICZ-C15 appears to have an agglomerated mixture of spherical and rod-type shapes, which is also confirmed on the FESEM image. The TEM images of ZnO appear to have an agglomerated, spherical-type morphology (Fig. 4.9a). According to the XRD pattern analysis, the particle sizes for ZnO and ICZ-C15 were 20–30 nm and 30–60 nm, respectively. From the HRTEM analysis, the

ZnO crystal's d-spacing value, which corresponds to the ZnO-NPs (002) crystallographic plane, is 0.285 nm (Fig. 4.9c, inset image). Besides, the lattice fringe values of 0.292, 0.271, and 0.220 nm, which also match the (002), (104), and (200) crystal planes of ZnO, Fe_2O_3, and CuO NPs, respectively, were validated by the HRTEM picture for ICZ-C15 (Fig. 4.9d, inset image) (Abebe et al., 2023; X. Liu et al., 2014; Park et al., 2012). The distortion created on the ICZ-C15 caused by the addition of copper and iron as dopants in the ZnO lattice was confirmed by the slight difference in the ZnO crystallographic plane lattice fringe value between single ZnO NPs and the ICZ-C15 (Kazmi et al., 2021; Majeed Khan et al., 2020). The more crystalline properties of the ICZ-C15 crystal than those of ZnO were further confirmed by the SAED ring analysis (Fig. 4.9e and f). The XRD pattern analysis results of ZnO and ICZ-Z15 materials are also displayed as an inset in Fig. 4.9e and f.

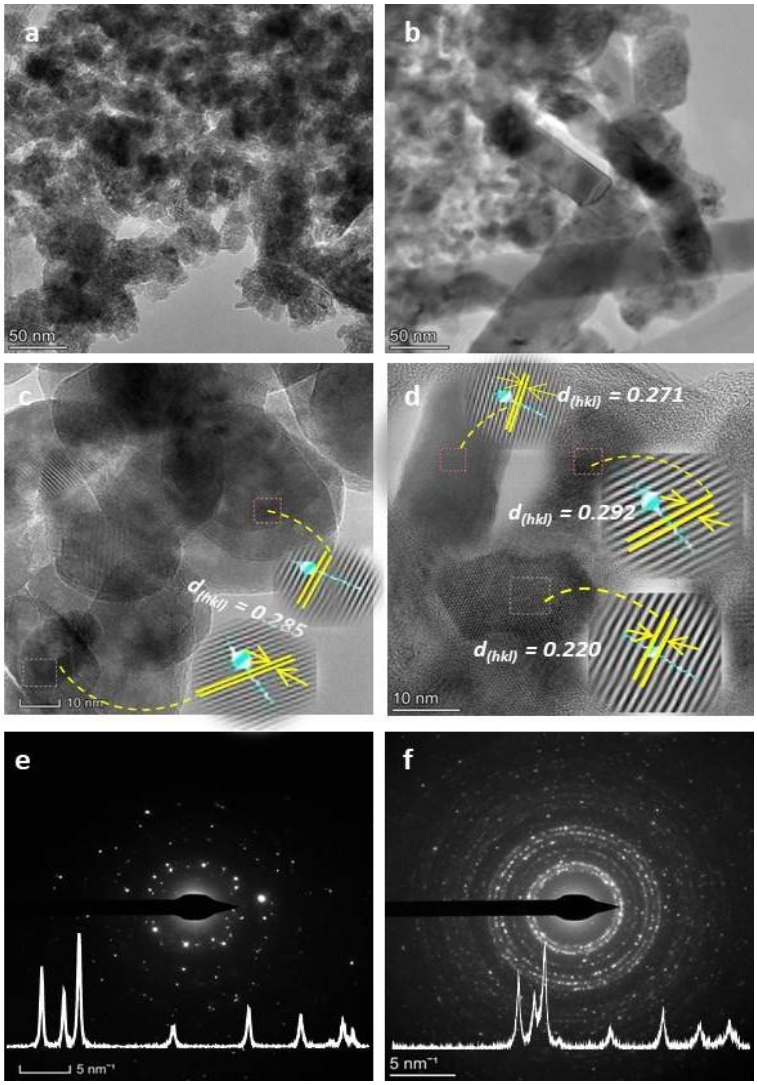

Figure 4.9. ZnO NPs and ICZ-C15 morphology, particle size, and crystallinity investigation using TEM/HRTEM/SAED techniques; (a and b) TEM, (c and d) HRETM, and (e and f) SAED images for ZnO NPs and ICZ-C15, respectively. The XRD patterns of ZnO NPs and ICZ-C15 are shown as insets in Fig. 19e and 19f, respectively.

4.5. Optical Property Analysis

Materials' optical properties were analyzed by photoluminescence (PL) and ultraviolet-visible diffuse reflectance (UV-vis-DRS) spectroscopy. Fig.4.10 shows the PL spectra of DMSO-suspended ZnO NPs, ICZ-C5, and ICZ-C15. Fig.4.11 shows the DRS-UV-vis spectra of powdered ZnO NPs and ICZ-C15. As shown in the PL spectrum of ZnO (Fig. 4.10a), it has an emission band at a maximum wavelength (λ_{max}) of 389 nm, which is mainly attributed to the near-band edge (NBE) transition. The NBE transition is one of the characteristic properties of ZnO, and it occurs due to electron-hole recombination.

The ICZ-C5 also showed the ZnO characteristics of NBE emission at 389 nm and slight violet emission at the λ_{max} value of 444 nm. The ICZ-C5 emission spectra were further deconvoluted for clarity, as shown in Fig. 4.10b. The occurrence of the violet emission is due to the iron-and-copper doping in the ZnO lattice as a result of electron-hole recombination from the iron-and-copper shallow level to the valance band of ZnO (Islah-u-din et al., 2020). Compared to the ZnO and ICZ-C5 emission spectra, the spectrum for ICZ-C15 showed an NBE band red shift towards 417 nm. This redshift emission is due to the independent low-band gap copper oxide or iron oxide emission (see the inset ICZ-C15 magnified view spectrum for clarity). The composite spectra peak showed a greater intensity reduction compared to ZnO. This intensity reduction for the nanocomposites indicates the presence of electron-hole recombination hindrance as a result of copper and iron impurity inclusions (Khan et al., 2020). The formation of a deep acceptor centre due to the iron and copper doping in the ZnO bandgap, which results in the quenching of luminescence, was also reported (Agarwal et al., 2019; Samanta et al., 2020). Electrons and holes have greater importance in generating highly oxidizing agents, hydroxyl radicals, by reacting with oxygen and water for catalysis applications (K. Xu et al., 2017; M. Xu et al., 2020).

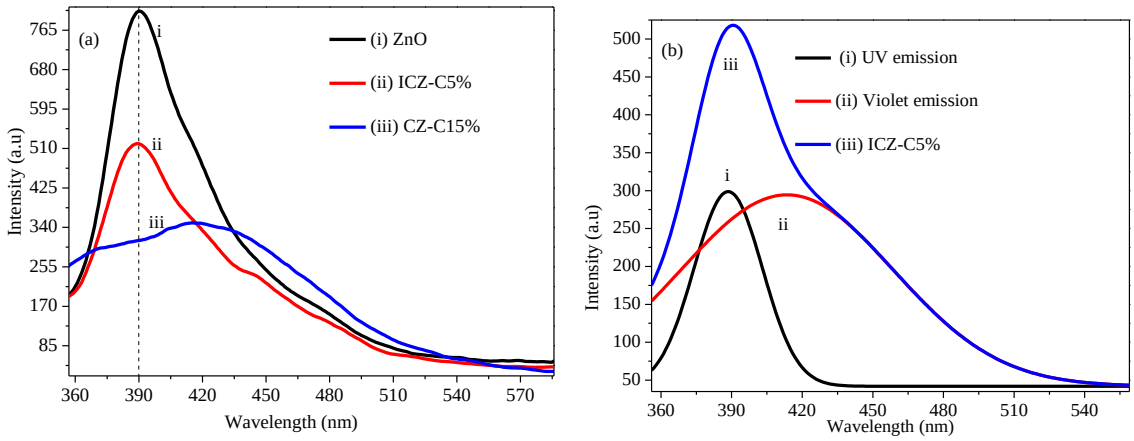

Figure 4.10. The photoluminescence spectra of ZnO and ICZ-C materials: (a) The PL spectra of ZnO, ICZ-C5, and ICZ-C15: (b) The deconvoluted ICZ-C5 emission spectrum.

In addition to the PL analysis, the optical properties of ZnO NPs and ICZ-C15 were analyzed by the DRS-UV-vis technique, as shown in Fig. 4.11. In this DRS-UV-vis analysis, the ZnO NPs showed better reflection properties than the composite. The greater light absorption property of the ICZ-C15, which is due to the *d-d* shallow level electron transition as a result of doping, is beneficial in the enhancement of the catalytic potential of the catalyst. The crucial semiconductor properties, namely the energy bandgap, were deduced using the Kubelka-Munk (K-M) plot analysis. Fig. 4.11b is the direct K-M function plot, in which the maximum valence band and minimum conduction band values, *k-factor* (crystal momentum), are equal, resulting in the direct emission of the pre-absorbed light. While Fig. 4.11c is the indirect K-M function, in which direct emission did not occur due to the difference in the crystal momentum values of the minimum conduction band and maximum valance band (Schneider, 2020). Catalysis applications prefer the indirect case. The relaxation of electrons and holes without recombination for some time results in reactions with oxygen and water, respectively, and generates an oxidizing agent called the hydroxyl radical. Materials' direct and indirect bandgap values are determined by interpolating the K-M function plots towards the x-axis. The direct and indirect bandgap values for ZnO were obtained to be 3.23 and 3.18 eV, respectively. The ICZ-C15 has direct and indirect bandgap values of 3.19 and 3.08 eV, respectively. The only slight change in optical properties between ZnO and ICZ-C15 on this DRS-UV-vis analysis is consistent with the XRD analysis, in which only a small percentage (up to 1%) of copper doping occurred. Besides, the substitution of dopant iron (III) in the host Zn (II) lattice shifts the host Fermi level near its conduction band, which results in a slight increase in the band gap (Samanta et al., 2020).

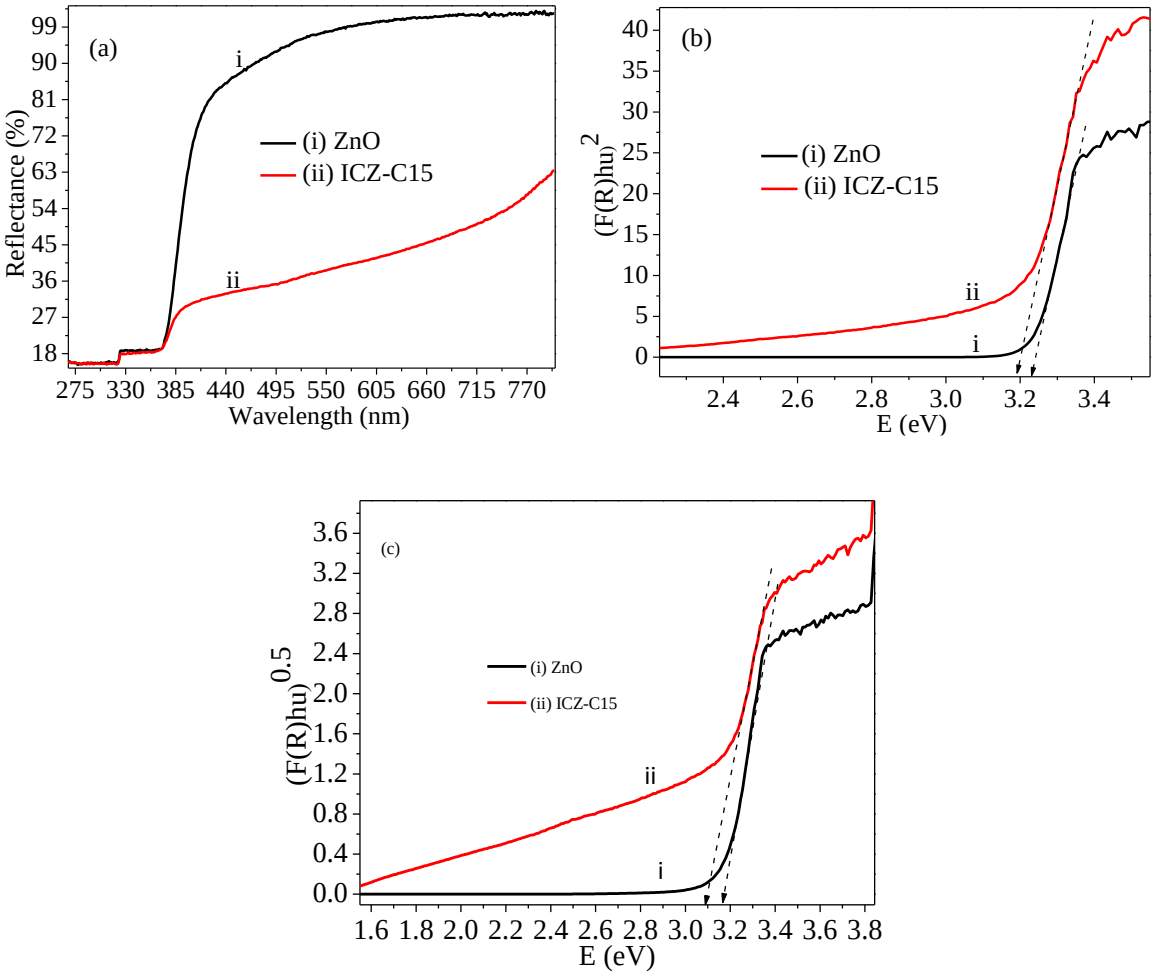

Figure 4.11. The UV-vis-DRS spectra of ZnO and ICZ-C15 materials: (a) The UV-vis-DRS spectra of ZnO and ICZ-C15. (b and c) are the direct and indirect Kubelka-Munk (K-M) plots.

4.6. Fourier Transform Infrared Spectroscopy (FT-IR) Analysis

The chemical binding and functional group analysis for calcined ZnO NPs, uncalcined ICZ-C15, and calcined ICZ-C15 were analyzed by the FTIR spectroscopic techniques, as shown in Fig. 4.12. Fig. 4.12a shows the presence of an intensity change between the calcined and uncalcined ICZ-C15. The uncalcined composites have greater intensity compared to the calcined ones. The broad absorption band that appeared at a wavenumber of 1380 and 3440 cm^{-1} is due to the H-O-H bending and O-H stretching vibrations, respectively, of the interstitial or surface-adsorbed water molecules. The intensity of these water molecule vibrations was reduced compared to the uncalcined ICZ-C15, indicating the presence of greater water molecule removal during calcination. Besides, there are also wavenumber shift

differences between the calcined and uncalcined composites (see Fig. 4.12b), in which the higher wavenumber shift for the calcined is due to the metal-oxygen bond stiffness compared to the uncalcined one (Lan et al., 1993). Of course, as reported in the Hong et al. study, the observed shift could also be attributed to PVA passivation (complex formation between PVA and salt precursor) (Hong et al., 2009). The band detected at about 540 cm^{-1} is the bending vibration of (Zn, Fe, or Cu)-O, due to the optical transverse bending vibration (transverse optical and longitudinal optical phonon frequencies) (Yang et al., 2010). As seen from the spectra (Fig. 4.12b, shown by the rectangle), after calcination, the metal-oxygen bond was clearly detected. The observed characteristic peaks for the uncalcined ICZ-C15 at 840 and 1470 cm^{-1} are due to the PVA CH_2 vibrations (Huang et al., 2016; Sudha et al., 2012). The source for the other peaks is probably due to the vibration of adsorbed carbon dioxide molecules or to the precursor intermediates left during synthesis (Anžlovar et al., 2011).

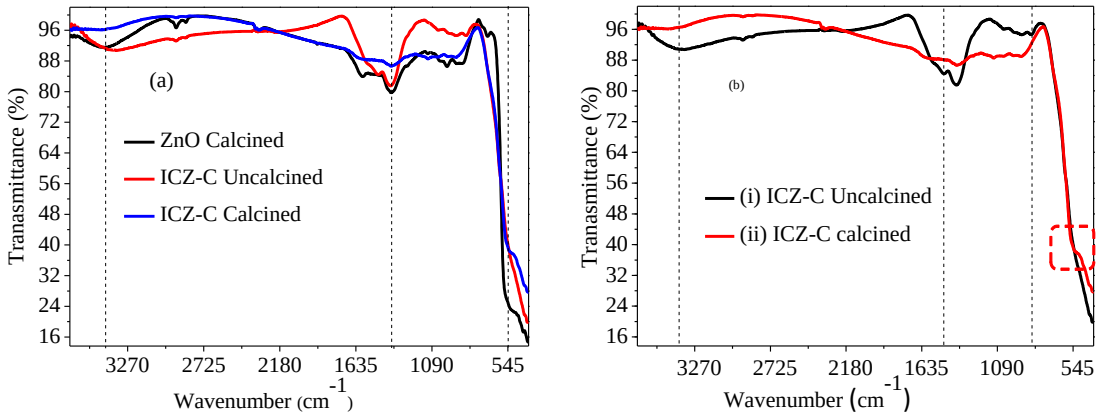

Figure 4.12. The FTIR spectroscopic chemical bonding analysis: (a) the FTIR spectra of ZnO NPs and ICZ-C15 before and after calcination (b) The spectrum for ICZ-C15 before and after calcination.

4.7. Catalytic Pollutant Reduction

4.7.1. Methylene Blue Catalytic Reduction

The catalytic reduction properties of MB into leuco-methylene blue (LMB) were studied, as shown in Fig. 4.13. The catalytic reduction result of ZnO NPs and ICZ-C15 in the presence of $NaBH_4$ is shown in Fig. 4.13(a-c). The MB has characteristic peaks at about 662, 610, and 291 nm, mainly due to the n-to-$\pi*$ transition in the later band (Basu et al., 2012). The reduction behaviour of MB to LMB was controlled spectroscopically by the decrease in the absorption maxima of MB at 662 nm and visually by color bleaching. Fig.

4.13a shows the spectra for MB before and after the addition of $NaBH_4$ (without catalyst), which show no noticeable changes. The absence of change in the absorption maxima indicates the absence of a reduction reaction in the presence of only $NaBH_4$.

The MB catalytic reduction results in the presence of a ZnO catalyst showed reduction but with less potential, probably due to its lower light absorption capacity, wider bandgap, and photon-induced electron-hole recombination. The observed slight catalytic properties of ZnO NPs were probably assisted by interstitial defects created during combustion or gas evolution (Nadupalli et al., 2021). These limitations observed in the ZnO NPs were clearly confirmed by the improved catalytic properties of doped materials. As shown in Fig. 4.13c ICZ-C15 resulted in an enhancement of the catalytic reduction reaction. The complete disappearance of the blue colour to colourless indicates the complete reduction reaction of MB to LMB. Percentage degradation of pure ZnO and ICZ-C15 were 20.4 % and 82.2 %, respectively as shown in Fig.4.13d. The reverse reaction (clock reaction) was also conducted by adding dilute 0.01 M NaOH, during which the LMB was converted to the MB within 5–10 seconds. This reversible reaction was not determined spectroscopically due to its promptness. The MB-to-LMB reduction took place here due to the presence of a $NaBH_4$-reducing agent and a catalyst to speed up the reaction. The transfer of electrons from the borohydride ion (BH_4^-) to the MB^+ was reported (Naseer et al., 2022; Ray et al., 2013) as the main mechanism for MB-to-LMB reduction.

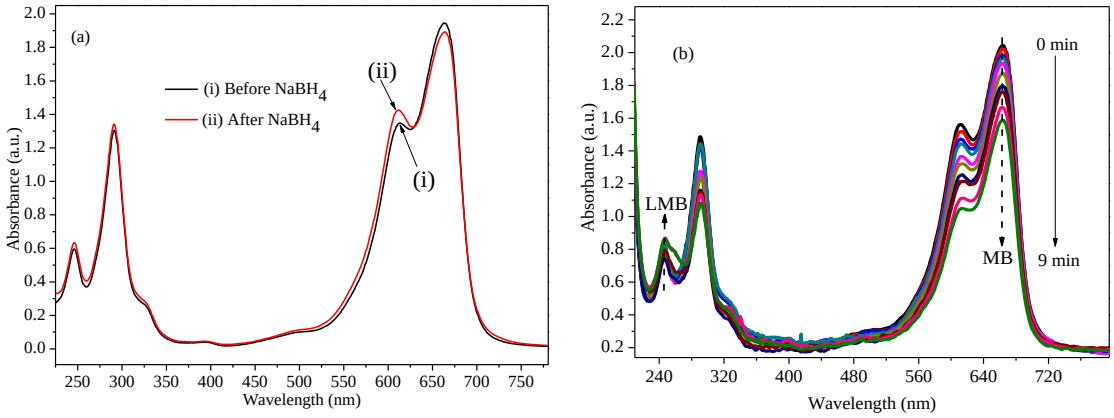

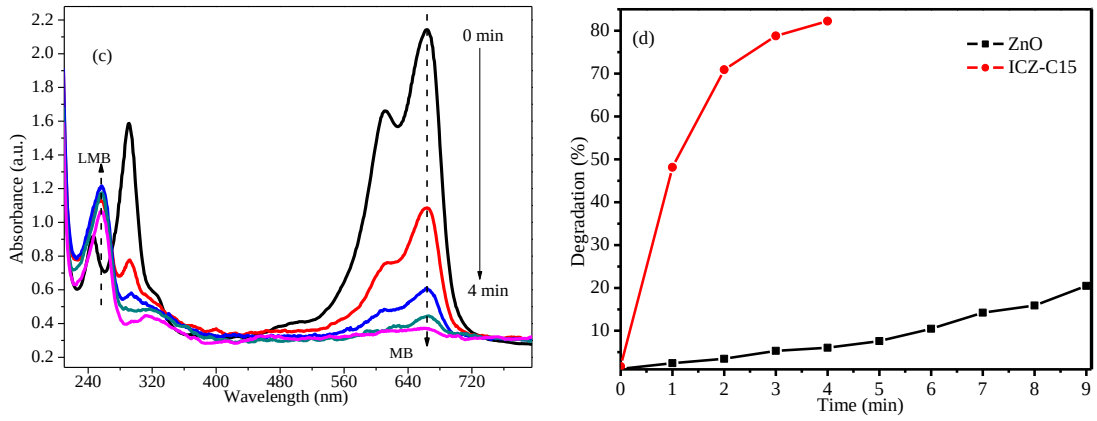

Figure 4.13. Catalytic reduction reaction for NPs and NCs in the presence and absence of $NaBH_4$: (a) the methylene blue spectrum in the presence and absence of $NaBH_4$; (b) the Methylene blue reduction result in the presence of $NaBH_4$ and ZnO NPs; (c) the reduction result in the presence of $NaBH_4$ and ICZ-C15 dopant; and (d) percentage degradation versus time plots of ZnO and ICZ-C15.

4.7.2. 4-Nitrophenol Catalytic Reduction

The thermodynamically possible 4-NP into 4-aminophenol (4-AP) catalytic reduction reaction can be catalyzed in the presence of a catalyst (Naseer et al., 2022). The catalytic reduction results of 4-NP into 4-AP in the presence of ZnO NPs and ICZ-C15 are shown in Fig. 4.14b and 4.14c, respectively. During the experiment, adding the $NaBH_4$ first results in a yellowish colour as a result of nitrophenolate ion formation and may release moderate bubbles. However, the reduction of 4-NP into 4-AP was not observed on the addition of $NaBH_4$, indicating a kinetically restricted reaction (Baruah et al., 2013). Besides, addition of ZnO NPs resulted in only a slight catalytic process, probably defects-assisted catalysis (Nadupalli et al., 2021), which is much lower than that of the composite. Here in the 4-NP into 4-AP catalytic reduction process, the ICZ-C15 was tested. As shown in Fig. 4.14d percentage degradation of pure ZnO and ICZ-C15 were 17.29 % and 99.13 %, respectively.

The superior catalysis for the ICZ-C15 with huge bubble formation is probably due to the improvement in the key catalysis parameters such as (i) optoelectrical properties, (ii) greater charge transfer properties due to doping and heterojunction, and (iii) enhanced surface area due to iron and copper. The complete diminishing of the 4-nitrophenolate ion (4-NP ion) peak at 400 nm and the appearance of the peak at 300 nm, as well as the entire colour fade, confirm the reduction of 4-NP into 4-AP. Here, during the reduction process, the catalyst acts as an electron transfer substrate from BH_4^- to 4-NP ions as BH_4^- is reduced to BO_3^- by releasing an electron (Abay et al., 2017; Naseer et al., 2022). In addition to the electrons,

hydrogen is also released from BH_4^- ($BH_4^- + 2H_2O \rightarrow BO_2^- + 4H_2$) and adsorbed by the nitro groups of 4-NP ions on the surface of the catalyst. Then continued hydro deoxygenation and release of water molecules took place to generate the 4-AP. In the first two-step absorption of hydrogen by oxygen from the nitro group, this results in the formation of intermediates. Finally, the formation of 4-aminophenol with the absorption of more hydrogen occurs (Kong et al., 2017). The 4-AP formation occurs after the formation of the hydroxyl aminophenol intermediate, which is transition state (Z. Wang et al., 2017).

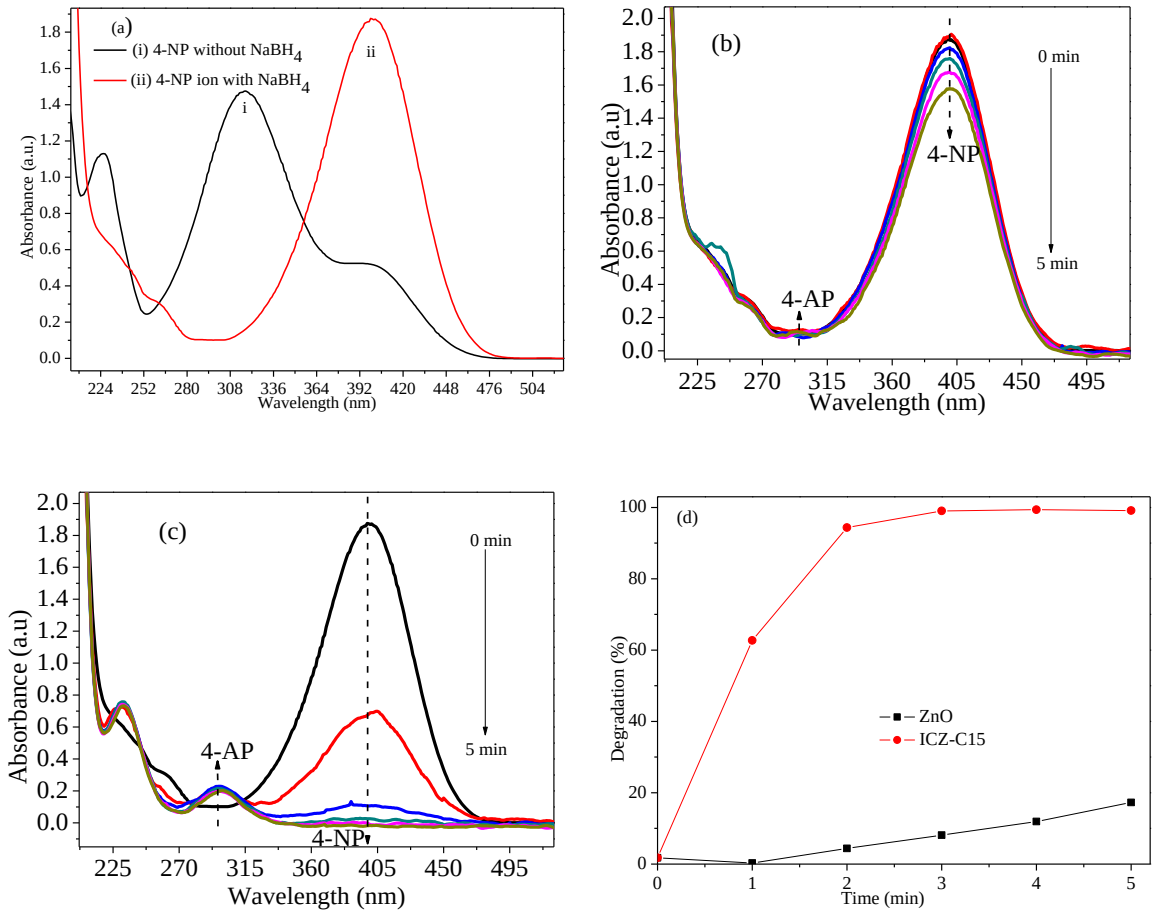

Figure 4.14 Catalytic reduction reaction for NPs and NCs in the absence and presence of NaBH4: (a) the 4-nitrophenol spectrum in the absence and presence of $NaBH_4$ (b) reduction of 4-nitrophenol to 4-aminophenol in the presence of $NaBH_4$ and ZnO NPs and (c) the reduction result in the presence of $NaBH_4$ and ICZ-C15; and (d) percentage degradation versus time plots of ZnO and ICZ-C15.

4.8. Photocatalytic Activity

More surface defects on the porous NCs increase photocatalytic degradation activity and light absorption efficiency (Tian et al., 2019). It is common knowledge that exposing a ZnO photocatalyst to radiation of sufficient energy results in the formation of electron and hole

pairs on the surface of the photocatalyst. The electrons interact with oxygen on the reduction of half-reaction ions to produce superoxide radicals, consequently producing the highly oxidizing agent, hydroxide radicals. Besides, the hole interacts with water in the oxidation half-reaction and generates more hydroxide radicals. However, the band potential of the photocatalyst determines whether these two reactions take place. When pollutants are adsorbed, the hydroxide radical oxidizing agent interacts with them and converts them to harmless minerals. However, an issue with electron-hole recombination may arise when using a single ZnO as a photocatalyst. This recombination issue, which is more pronounced in the nanoscale range, reduces their quantum efficiency and may also trigger extremely desired reactions and have implications for the dissipation of radiant energy (Lachheb et al., 2017). Doping and the creation of an interface between two or more metal oxide semiconductors are two of the many methods discovered to enhance the photocatalysts' capacity for charge transfer (Jiamprasertboon et al., 2019; Mohd Adnan et al., 2016).

On methylene blue dye, the photocatalytic activity of both ZnO NPs and ICZ-Cs was noble. ICZ-Cs strong photocatalytic abilities may be attributed to the interstitial vacancy during combustion, which diminishes electron or hole recombination. However, contrary to expectations, the photocatalytic activities of ZnO NP's are not as superior as those of composites. Fig. 4.15 displays the ZnO NPs and ICZ-Cs degradation activities on methylene blue dye. In general, the photocatalytic activity of ICZ-Cs was better than ZnO NPs. As seen from Fig. 4.15, ICZ-C15 sample exhibits the highest photocatalytic activity (90.23%), compared to ZnO (39.09%), ICZ-C1 (73.3%), and ICZ-C10 (73.66%) within 100 minute degradation time. This may be due to the smaller bandgap and creation of electron trap level which prevents recombination (Gusain et al., 2020).

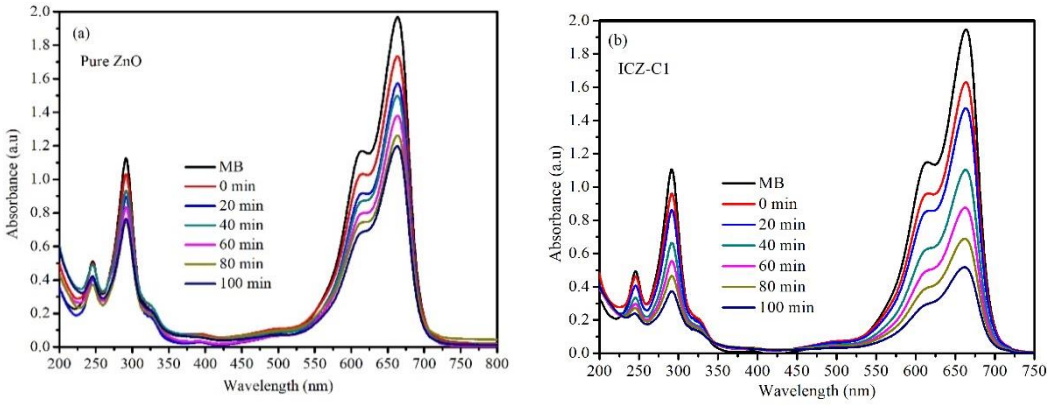

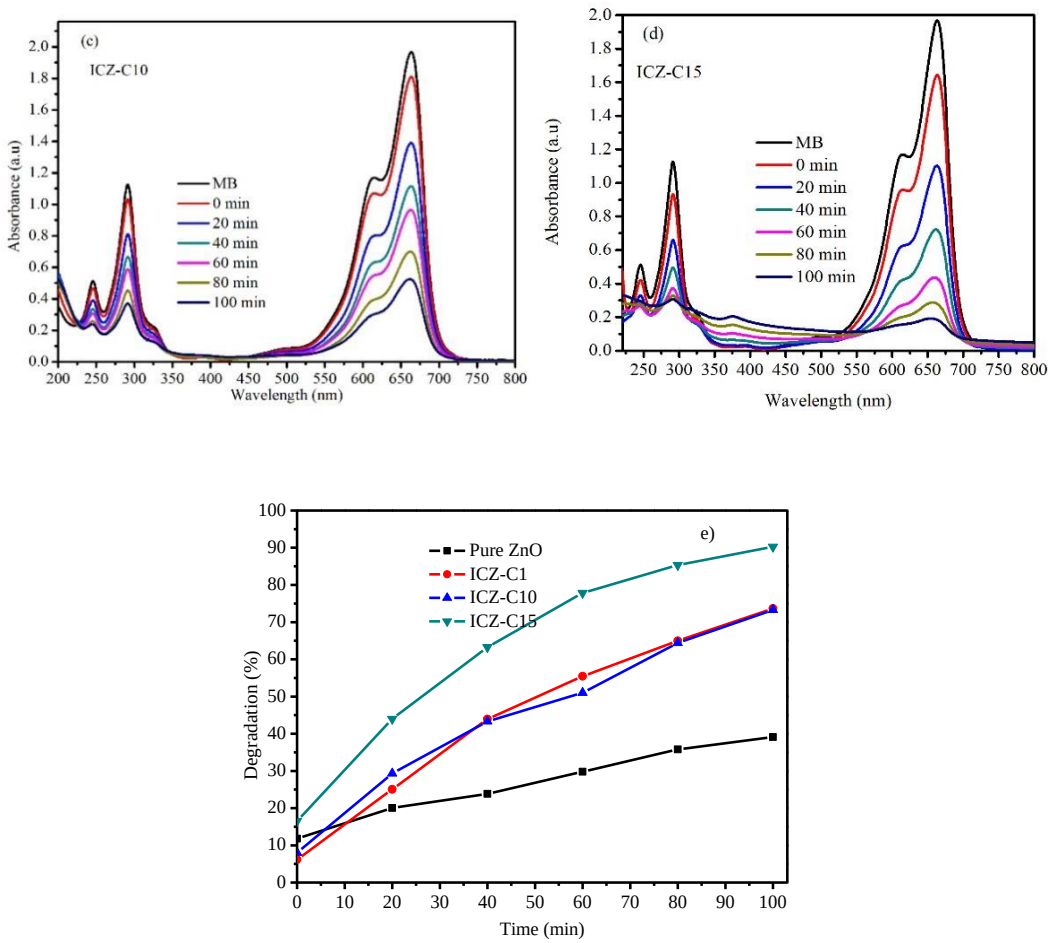

Figure 4.15. Absorbance versus wavelength plots of a) pure ZnO NPs, b) ICZ-C1, c) ICZ-C10, d) ICZ-C15, e) percentage degradation versus time plots of ZnO NPs, CZ-C1, ICZ-C10, and ICZ-C15.

Fig. 4.16 shows the pseudo-first and second -order kinetics linear curve of pure ZnO, ICZ-C1, ICZ-C10, and ICZ-C15. From kinetics order graph pseudo- first- order kinetics is preferable with greater correlation coefficient value of 0.96843 as compared to pseudo-second-order kinetic. The highest degradation rate constant was 0.02956 min^{-1} for ICZ-C15 indicates its greater efficacy owing to its lower electron-hole recombination property and effective charge separation property (Prabakaran & Pillay, 2019).

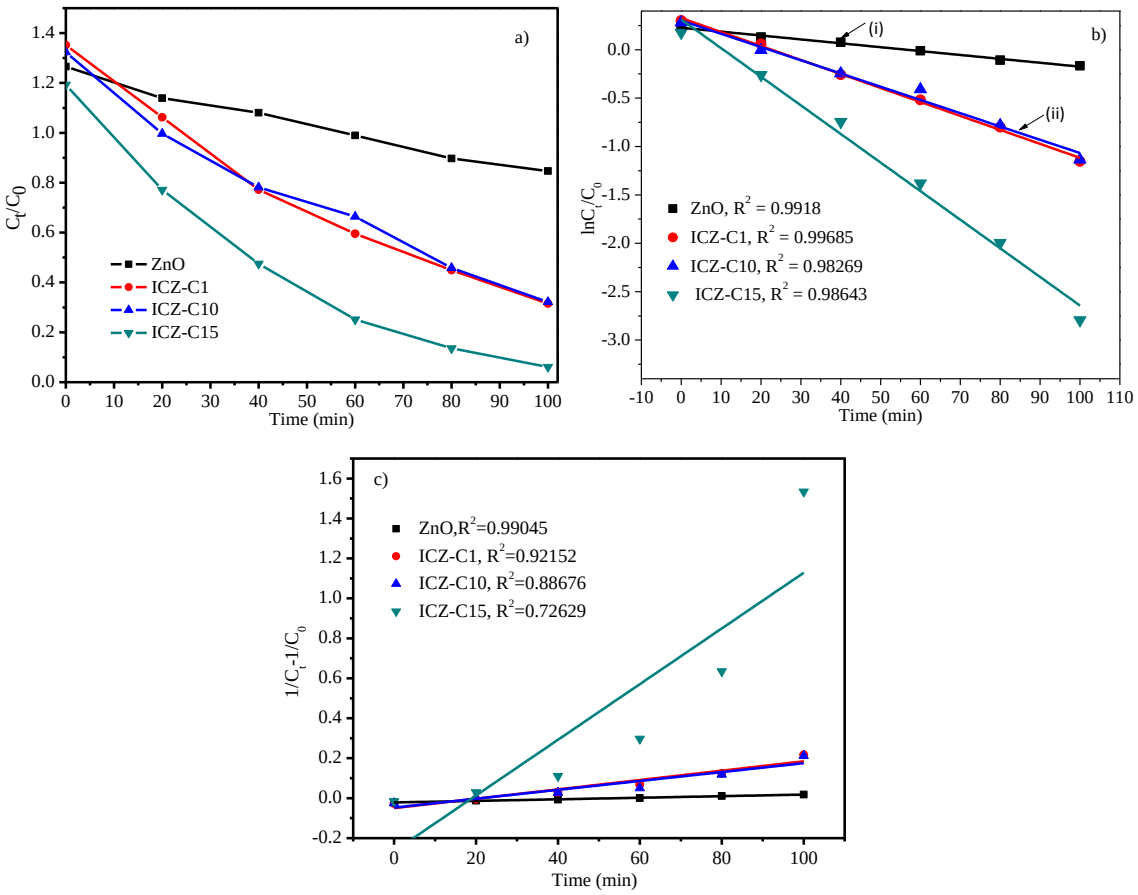

Figure 4.16 (a) C_t/C_o versus time degradation and (b) ln C_t/C_o versus time pseudo-first-order kinetics linear plots of pure ZnO NPs, ICZ-C1, ICZ-C10, and ICZ-C15; and (c) Pseudo-second –order kinetics linear plots .

4.8.1. Dosage Effect

Figure 4.17 shows catalyst dosage amount optimization for ICZ-C15, ranging from 10 mg to 50 mg. The degradation efficiency of MB increases from 10 mg to 20 mg and decreases from 30 mg to 50 mg. The highest kinetic rate constant (0.0306 min^{-1}) and correlation coefficient (0.98643) at 20 mg catalyst were obtained as presented in Table 4.1. As shown in Fig.4.18 pseudo-first-order kinetics shows highest correlation coefficient (R^2=0.98643) as compared to second order kinetics. One of the potential causes for decreasing the catalytic activity after 20 mg could be the turbidity of the solution as a result of the increase in the amount of catalyst, which prevents radiation from entering the solution. Another factor could be the agglomeration of high concentrations of nanoparticles in the solution, which limits the number of active surface sites that are open to exposure (Gusain et al., 2020).

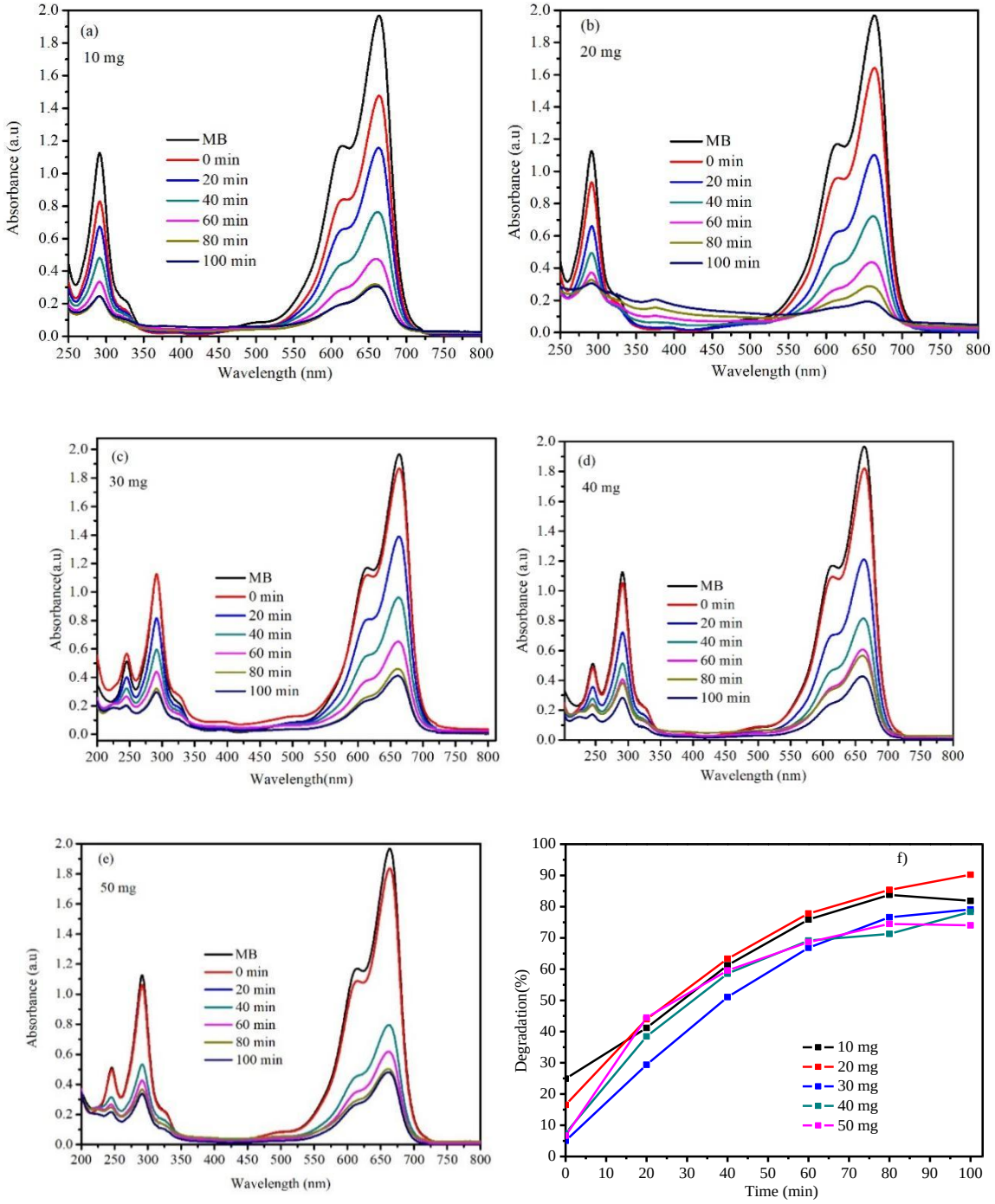

Figure 4.17 Absorbance versus wavelength plots of catalyst ICZ-C15 a) 10 mg, b) 20 mg, c) 30 mg, d) 40 mg, d) 50 mg, and f) is the percent degradation versus time plot of catalyst dosage.

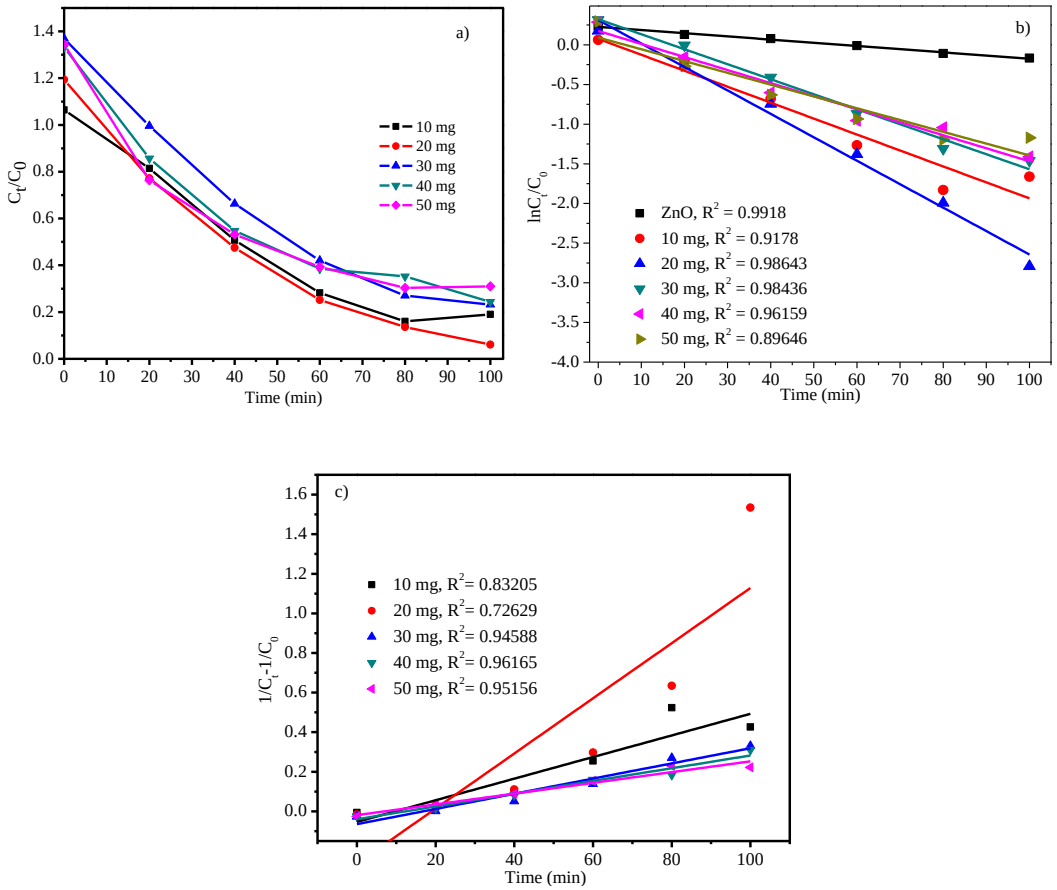

Figure 4.18 a) C_t/C_o versus time plot of dosage, and b) ln C_t/C_o versus time pseudo-first-order kinetics linear plots catalyst dosage, and c) pseudo-second-order kinetics plot.

4.8.2. pH Effect

The pH of the solution is a critical factor for pollutant degradation (ref). Solution pH optimization (3, 5, 9, and 11) for the ICZ-C15 catalyst was studied using HCl and NaOH for pH adjustment, as shown in Fig. 4.19. Fig. 4.20 displays the percentage degradation efficiency, Ct/Co versus time, and ln Ct/Co pseudo-first and second -order kinetics linear plots. In acidic media, both MB and ICZ-C15 catalysts have a positive charge, which results in repulsion towards one another. Thus, there was not complete degradation at pH 3 or pH 5. However, at higher values of pH 9 and pH 11, the degradation efficiency increased as a result of electrostatic attraction between the negatively charged ICZ-C15 catalyst and the positively charged MB (Table 1) (Prabakaran & Pillay, 2019).

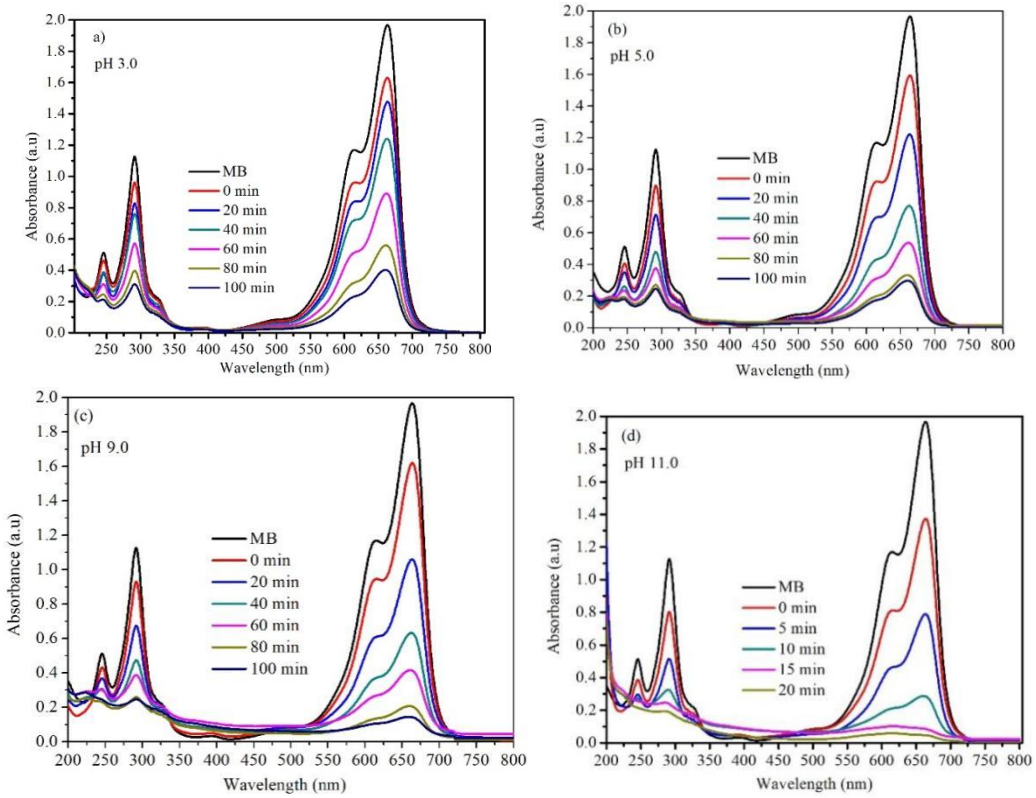

Figure 4.19 Absorbance versus wavelength plots of catalyst ICZ-C15 a) pH 3.0, b) pH 5.0, c) pH 9.0, and d) pH 11.0

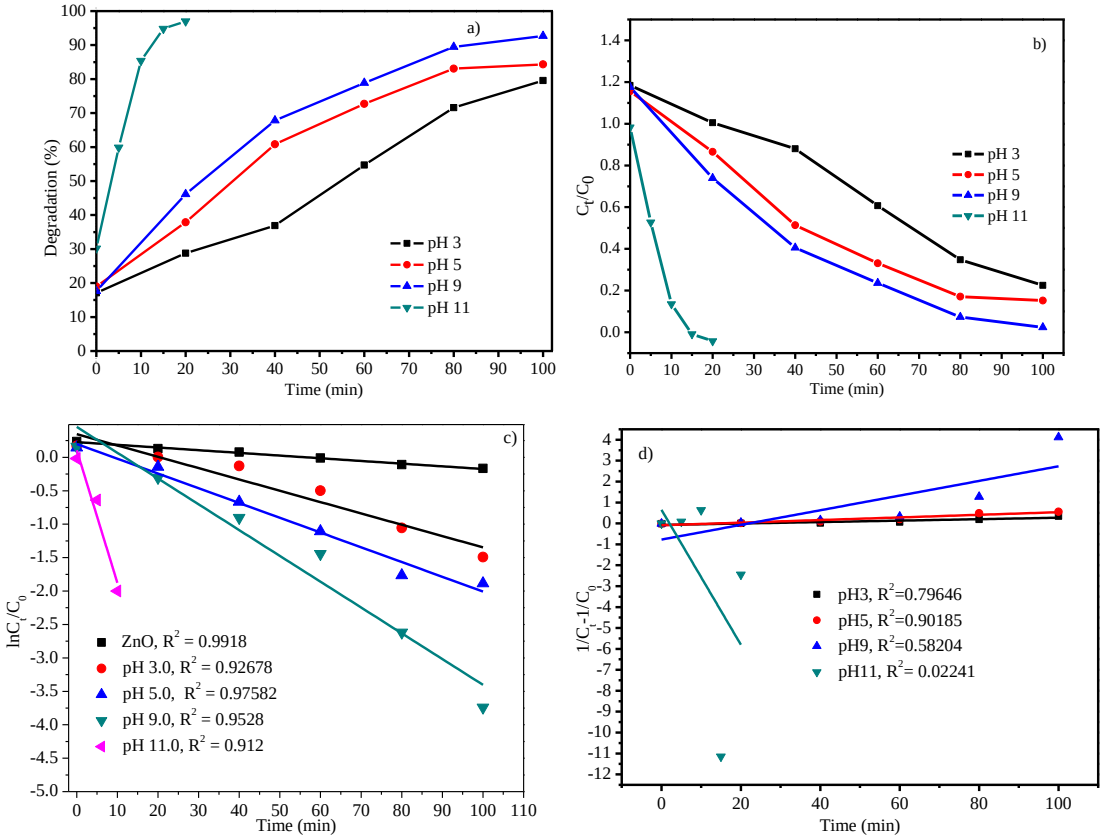

Figure 4.20. a) percent degradation versus time plot of pH 3,5,9, and 11 ;b) C_t/C_o versus time plot of pH 3,5,9, and 11 and c) ln C_t/C_o versus time pseudo-first-order kinetics linear plots of pH 3,5,9, and

4.8.3. Concentration Effect

The initial dye concentration is the other factor that influences the photocatalytic degradation activity of pollutants (Gusain et al., 2020). Fig. 4.21 shows the photocatalytic degradation of MB in the presence of ICZ-C15 catalyst with various initial dye concentrations (5 ppm, 10 ppm, and 15 ppm) under light irradiation. The experiment was conducted by taking the optimum 20 mg of ICZ-C15 catalyst dosage and solution pH values of 11. The highest deterioration was achieved at 10 ppm, with the highest degradation efficacy of 97%. The obtained rate constant was 0.19828 $min^{-1}$with a correlation coefficient value of 0.91204, as illustrated in Fig. 4.22b and Table 4.1. Due to the production of OH• radical on the catalyst's surface and the reaction between the dye molecule and OH• radical, the efficiency of degradation improved as the initial dye concentration increased. However, additional increases in the initial dye concentration cause the catalyst's activity to diminish because the reaction between the dye molecule and the OH• radical is inhibited when more dye adsorbs to the surface of the catalyst, which lowers the generation of the OH• radical (Anju Chanu et al., 2019). The concentrations of the photocatalytic activities were determined from the calibration curve by taking concentrations from 0 ppm to 16 ppm by the serial dilution method, as shown in Figs. 4.23a and b. As seen from Fig. 4.23b, there is some deviation at higher concentrations due to the individual particles of the analyte no longer being independent of each other, resulting in interaction between them and a smaller absorptivity than expected.

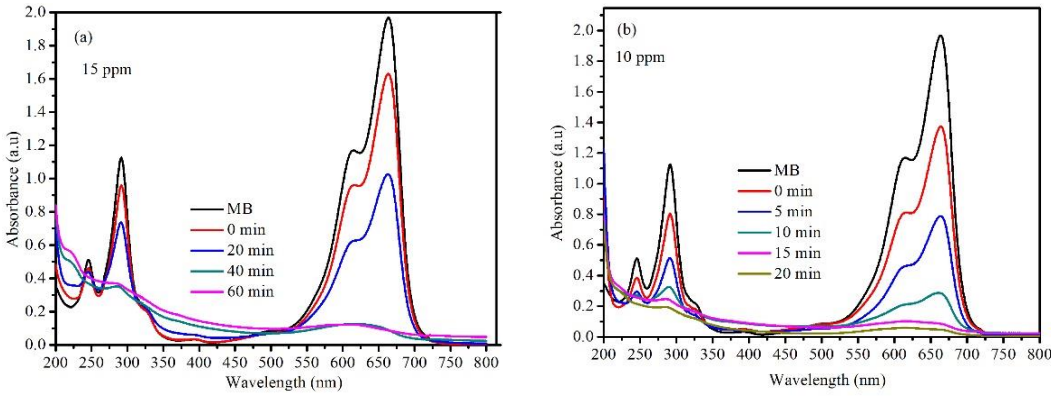

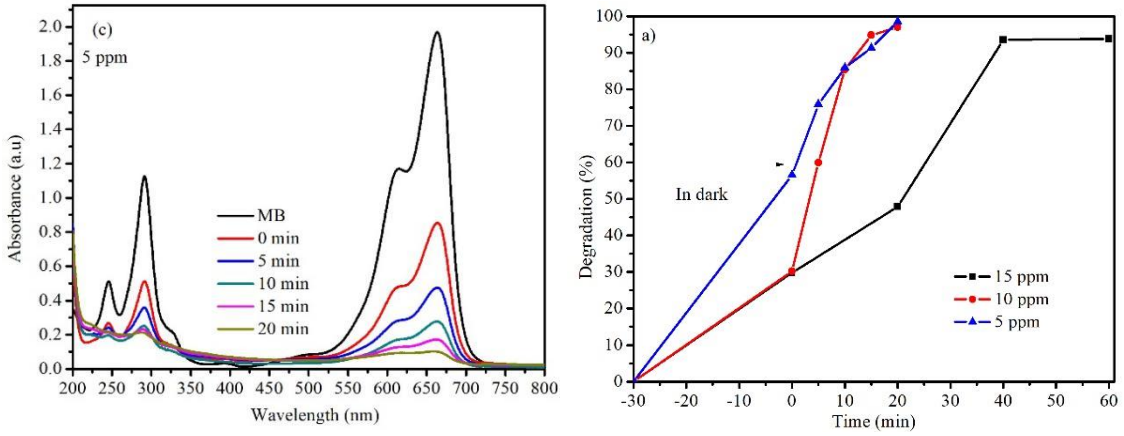

Figure 4.21. Absorbance versus wavelength plots of catalyst ICZ-C15 a) 15 ppm, b) 10 ppm, and c) 5 ppm ; d) percent degradation versus time plot of 15 ppm, 10 ppm, and 5 ppm

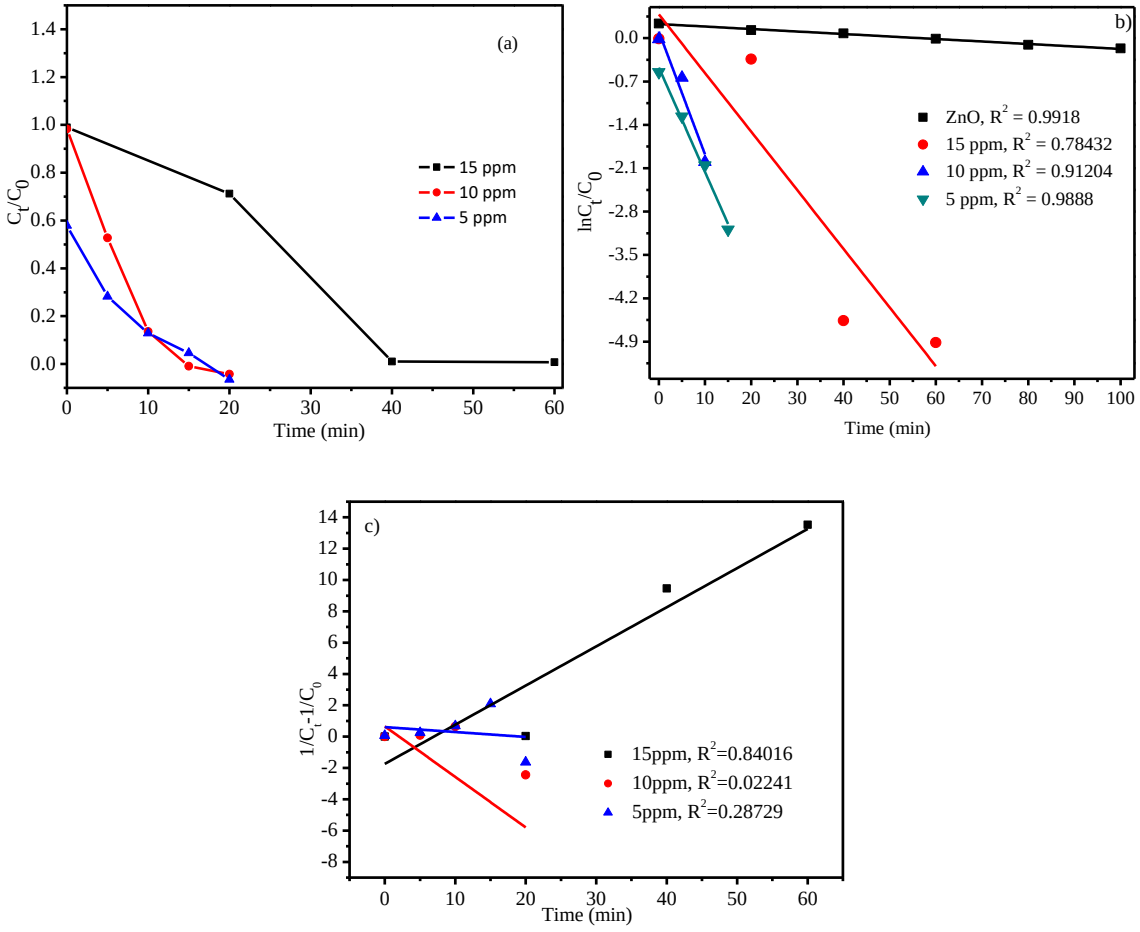

Figure 4.22. a) C_t/C_o versus time plot of 15 ppm, 10 ppm, and 5 ppm; b) ln C_t/C_o versus time pseudo-first-order kinetics linear plots of 15 ppm, 10 ppm, and 5 ppm.

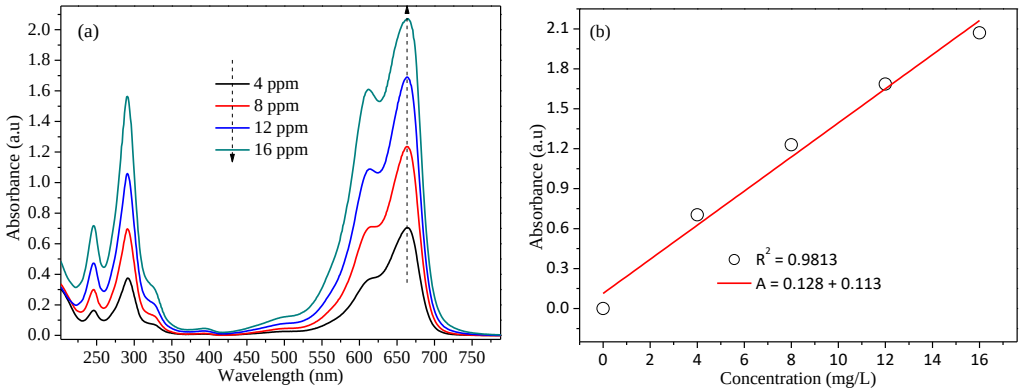

Figure 4.23 (a) Absorbance versus wavelength spectrum plots of methylene blue dye; (b) absorbance versus concentration calibration curve

Table 4.1 Percentage degradation efficiency, kinetic rate constant, and correlation coefficient of composites, catalyst dosage, pH of the solution, and initial concentration of the dye.

Composites						
	Pure ZnO	ICZ-C1			ICZ-C10	ICZ-C15
PDE %	39.09	73.3			73.6	90.23
K(min^{-1})	0.00402	0.01445			0.01368	0.02956
R^2	0.9918	0.99685			0.98269	0.98643
Catalyst dosage						
	Pure ZnO	10 mg	20 mg	30 mg	40 mg	50 mg
PDE %	39.09	81.85	90.23	79.1	78.34	74.02
K(min-1)	0.00402	0.02011	0.0306	0.01891	0.01644	0.01487
R^2	0.9918	0.9178	0.98643	0.98436	0.96159	0.89646
pH of the solution						
	ZnO	pH 3.0		pH 5.0	pH 9.0	pH 11.0
PDE %	39.09	79.56		84.34	92.67	97.0
K(min^{-1})	0.00402	0.01694		0.02207	0.03858	0.19828
R^2	0.9918	0.92678		0.97582	0.9528	0.912
Methylene blue concentration						
	ZnO	15 ppm			10 ppm	5 ppm
PDE	39.09	93.74			97	98.47
K(min-1)	0.00402	0.09466			0.19828	0.16823
R^2	0.9918	0.78432			0.91204	0.9888

5. CONCLUSIONS AND RECOMMENDATIONS

5.1. Conclusions

In conclusion, the precursor-polymer complex combustion synthesis approach is a crucial method for synthesizing porous doped materials with good dopant distributions. The absence of an independent iron peak, unlike that of copper on the XRD pattern, is due to ZnO's dominance. Both doping and heterojunction induce optoelectronic improvements for ZnO. The charge transfer developed due to doping and heterojunction has a crucial effect on the diminution of electron-hole recombination and on enhancing the materials catalytic properties. The catalytic 4-nitrophenol and methylene blue dye reduction properties of the doped composites showed elevated improvements over single ZnO 99.13% and 82.2% respectively. Besides, the catalytic properties of the methylene blue dye in the composite are much better than ZnO. The 90.23% degradation shows ICZ-C15 catalyst exhibits highest photocatalytic activities. From performance activity degradation of MB in aqueous solution gives highest percentage degradation efficiency as compared to the catalytic reduction activity of MB. Pseudo-first-order kinetics is suitable for photocatalytic activity with greater correlation coefficient (R^2) value as compared to pseudo-second-order kinetics value. Thus, this combustion method that needs a short time and less energy for materials synthesis in combination with a doping system has an evident future for pollutant remediation in industrial applications.

5.2. Recommendations

One of the popular methods for improving the photoactivity of semiconductor nanomaterials is semiconductor doping, which does so by boosting photon-capture effectiveness in the visible light spectrum. Many studies, including this one, give presumed proposals on doping inclusion and distribution. When interpreting data, various false assumptions and mistakes are routinely made that can produce erroneous conclusions concerning the impact of doping on catalysis. One of them is figuring out where the dopants are and their distribution. The difference between surface modification and bulk alteration can be difficult to identify. Thus, since the doping chemistry is not easily understandable by techniques such as XRD and SEAM, the authors recommend further studies using advanced techniques such as X-ray absorption spectroscopy (XAS) and Scanning transmission electron microscopy (STEM) with various detectors.

REFERENCE

Abay, A. K., Chen, X., & Kuo, D.-H. (2017). Highly efficient noble metal free copper nickel oxysulfide nanoparticles for catalytic reduction of 4-nitrophenol, methyl blue, and rhodamine-B organic pollutants. *New Journal of Chemistry*, *41*(13), 5628–5638. https://doi.org/10.1039/C7NJ00676D

Abebe, B., Kefale, B., & Leku, D. T. (2023). Synthesis of copper–silver–zinc oxide nanocomposites for 4-nitrophenol reduction: doping and heterojunction. *RSC Advances*, *13*(7), 4523–4529. https://doi.org/10.1039/D2RA07845G

Abebe, B., & Murthy, H. C. A. (2022). Insights into ZnO-based doped porous nanocrystal frameworks. *RSC Advances*, *12*(10), 5816–5833. https://doi.org/10.1039/D1RA09152B

Abebe, B., Tsegaye, D., & Ananda Murthy, H. C. (2022). Insight into nanocrystal synthesis: from precursor decomposition to combustion. *RSC Advances*, *12*(37), 24374–24389. https://doi.org/10.1039/D2RA05222A

Agarwal, D. C., Singh, U. B., Gupta, S., Singhal, R., Kulriya, P. K., Singh, F., Tripathi, A., Singh, J., Joshi, U. S., & Avasthi, D. K. (2019). Enhanced room temperature ferromagnetism and green photoluminescence in Cu doped ZnO thin film synthesised by neutral beam sputtering. *Scientific Reports*, *9*(1), 6675. https://doi.org/10.1038/s41598-019-43184-9

Alencar, L. V. T. D., Passos, L. M. S., Soriano, R. N., Bharagava, R. N., Ferreira, L. F. R., & de Souza, R. L. (2021). *Aqueous Two-Phase Systems: An Alternative Process for Industrial Dye Recovery*. 35–55. https://doi.org/10.1007/978-981-15-6564-9_3

Ali, S., Razzaq, A., Kim, H., & In, S.-I. (2022). Activity, selectivity, and stability of earth-abundant CuO/Cu2O/Cu0-based photocatalysts toward CO2 reduction. *Chemical Engineering Journal*, *429*, 131579. https://doi.org/10.1016/j.cej.2021.131579

Andreo, J., Ettlinger, R., Zaremba, O., Peña, Q., Lächelt, U., de Luis, R. F., Freund, R., Canossa, S., Ploetz, E., Zhu, W., Diercks, C. S., Gröger, H., & Wuttke, S. (2022). Reticular Nanoscience: Bottom-Up Assembly Nanotechnology. *Journal of the American Chemical Society*, *144*(17), 7531–7550. https://doi.org/10.1021/jacs.1c11507

Anju Chanu, L., Joychandra Singh, W., Jugeshwar Singh, K., & Nomita Devi, K. (2019). Effect of operational parameters on the photocatalytic degradation of Methylene blue dye solution using manganese doped ZnO nanoparticles. *Results in Physics*, *12*(December 2018), 1230–1237. https://doi.org/10.1016/j.rinp.2018.12.089

Anžlovar, A., Kogej, K., Crnjak Orel, Z., & Žigon, M. (2011). Polyol mediated nano size zinc oxide and nanocomposites with poly(methyl methacrylate). *Express Polymer Letters*, *5*(7), 604–619. https://doi.org/10.3144/expresspolymlett.2011.59

Bacaksiz, E., Parlak, M., Tomakin, M., Özçelik, A., Karakiz, M., & Altunbaş, M. (2008).

The effects of zinc nitrate, zinc acetate and zinc chloride precursors on investigation of structural and optical properties of ZnO thin films. *Journal of Alloys and Compounds*, *466*(1–2), 447–450. https://doi.org/10.1016/j.jallcom.2007.11.061

Bagheri, M., Melillo, A., Ferrer, B., Masoomi, M. Y., & Garcia, H. (2022). Quasi-HKUST Prepared via Postsynthetic Defect Engineering for Highly Improved Catalytic Conversion of 4-Nitrophenol. *ACS Applied Materials & Interfaces*, *14*(1), 978–989. https://doi.org/10.1021/acsami.1c19862

Baig, N., Kammakakam, I., Falath, W., & Kammakakam, I. (2021). Nanomaterials: A review of synthesis methods, properties, recent progress, and challenges. *Materials Advances*, *2*(6), 1821–1871. https://doi.org/10.1039/d0ma00807a

Baruah, B., Gabriel, G. J., Akbashev, M. J., & Booher, M. E. (2013). Facile Synthesis of Silver Nanoparticles Stabilized by Cationic Polynorbornenes and Their Catalytic Activity in 4-Nitrophenol Reduction. *Langmuir*, *29*(13), 4225–4234. https://doi.org/10.1021/la305068p

Basu, M., Sinha, A. K., Pradhan, M., Sarkar, S., Pal, A., Mondal, C., & Pal, T. (2012). Methylene Blue–Cu 2 O Reaction Made Easy in Acidic Medium. *The Journal of Physical Chemistry C*, *116*(49), 25741–25747. https://doi.org/10.1021/jp308095h

Bhagwat, V. R., Humbe, A. V., More, S. D., & Jadhav, K. M. (2019). Sol-gel auto combustion synthesis and characterizations of cobalt ferrite nanoparticles: Different fuels approach. *Materials Science and Engineering B: Solid-State Materials for Advanced Technology*, *248*(2), 114388. https://doi.org/10.1016/j.mseb.2019.114388

Buonsanti, R., & Milliron, D. J. (2013). Chemistry of doped colloidal nanocrystals. *Fe, Cu Co Doped ZnO*, *25*(8), 1305–1317. https://doi.org/10.1021/cm304104m

Carlos, E., Martins, R., Fortunato, E., & Branquinho, R. (2020). Solution Combustion Synthesis: Towards a Sustainable Approach for Metal Oxides. *Chemistry – A European Journal*, *26*(42), 9099–9125. https://doi.org/10.1002/chem.202000678

Chauhan, L., Shukla, A. K., & Sreenivas, K. (2016). Properties of NiFe2O4 ceramics from powders obtained by auto-combustion synthesis with different fuels. *Ceramics International*, *42*(10), 12136–12147. https://doi.org/10.1016/j.ceramint.2016.04.146

Chen, D., Sivakumar, M., & Ray, A. K. (2000). Heterogeneous photocatalysis in environmental remediation. *Developments in Chemical Engineering and Mineral Processing*, *8*(5–6), 505–550. https://doi.org/10.1002/apj.5500080507

Choudhary, S., Sarma, J. V. N., Pande, S., Ababou-Girard, S., Turban, P., Lepine, B., & Gangopadhyay, S. (2018). Oxidation mechanism of thin Cu films: A gateway towards the formation of single oxide phase. *AIP Advances*, *8*(5), 055114. https://doi.org/10.1063/1.5028407

Costa, A. C. F. M., Morelli, M. R., & Kiminami, R. H. G. A. (2007). Microstructure and magnetic properties of Ni1-x Zn x Fe2O4 synthesized by combustion reaction. *Journal of Materials Science*, *42*(3), 779–783. https://doi.org/10.1007/s10853-006-1440-6

Costas, A., Florica, C., Preda, N., Besleaga, C., Kuncser, A., & Enculescu, I. (2022). Self-connected CuO–ZnO radial core–shell heterojunction nanowire arrays grown on interdigitated electrodes for visible-light photodetectors. *Scientific Reports*, *12*(1), 6834. https://doi.org/10.1038/s41598-022-10879-5

Dai, Y., Tang, Q., Zhang, Z., Yu, C., Li, H., Xu, L., Zhang, S., & Zou, Z. (2018). Enhanced mechanical, thermal, and UV-shielding properties of poly(vinyl alcohol)/metal–organic framework nanocomposites. *RSC Advances*, *8*(67), 38681–38688. https://doi.org/10.1039/C8RA07143H

Deng, Y., Wei, J., Sun, Z., & Zhao, D. (2013). Large-pore ordered mesoporous materials templated from non-Pluronic amphiphilic block copolymers. *Chem. Soc. Rev.*, *42*(9), 4054–4070. https://doi.org/10.1039/C2CS35426H

Devan, R. S., Patil, R. A., Lin, J.-H., & Ma, Y.-R. (2012). One-Dimensional Metal-Oxide Nanostructures: Recent Developments in Synthesis, Characterization, and Applications. *Advanced Functional Materials*, *22*(16), 3326–3370. https://doi.org/10.1002/adfm.201201008

Dhiman, P., Naushad, M., Batoo, K. M., Kumar, A., Sharma, G., Ghfar, A. A., Kumar, G., & Singh, M. (2017). Nano Fe x Zn 1−x O as a tuneable and efficient photocatalyst for solar powered degradation of bisphenol A from aqueous environment. *Journal of Cleaner Production*, *165*, 1542–1556. https://doi.org/10.1016/j.jclepro.2017.07.245

Duan, K., Que, T., Koppala, S., Balan, R., Lokesh, B., Pillai, R., David, S., Karthikeyan, P., Ramamoorthy, S., Lekshmi, I. C., Kemacheevakul, P., Padmavathy, N., & Munusamy, S. (2022). A facile route to synthesize n-SnO 2 /p-CuFe 2 O 4 to rapidly degrade toxic methylene blue dye under natural sunlight. *RSC Advances*, *12*(26), 16544–16553. https://doi.org/10.1039/D2RA01690G

Dunne, P. W., Munn, A. S., Starkey, C. L., Huddle, T. A., & Lester, E. H. (2015). Continuous-flow hydrothermal synthesis for the production of inorganic nanomaterials. *Philosophical Transactions of the Royal Society A: Mathematical, Physical and Engineering Sciences*, *373*(2057). https://doi.org/10.1098/rsta.2015.0015

Dutta, S., Chattopadhyay, S., Sarkar, A., Chakrabarti, M., Sanyal, D., & Jana, D. (2009). Role of defects in tailoring structural, electrical and optical properties of ZnO. *Progress in Materials Science*, *54*(1), 89–136. https://doi.org/10.1016/j.pmatsci.2008.07.002

Dzhardimalieva, G. I., & Uflyand, I. E. (2018). Preparation of metal-polymer nanocomposites by chemical reduction of metal ions: functions of polymer matrices. *Journal of Polymer Research*, *25*(12), 47–49. https://doi.org/10.1007/s10965-018-1646-8

Espitia, P. J. P., Soares, N. de F. F., Coimbra, J. S. dos R., de Andrade, N. J., Cruz, R. S., & Medeiros, E. A. A. (2012). Zinc Oxide Nanoparticles: Synthesis, Antimicrobial Activity and Food Packaging Applications. *Food and Bioprocess Technology*, *5*(5), 1447–1464. https://doi.org/10.1007/s11947-012-0797-6

Fu, M., Li, Y., Wu, S., Lu, P., Liu, J., & Dong, F. (2011). Sol-gel preparation and enhanced

photocatalytic performance of Cu-doped ZnO nanoparticles. *Applied Surface Science*, *258*(4), 1587–1591. https://doi.org/10.1016/j.apsusc.2011.10.003

Gao, Y., Meng, F., Li, X., Wen, J. Z., & Li, Z. (2016). Factors controlling nanosized Ni–Al 2 O 3 catalysts synthesized by solution combustion for slurry-phase CO methanation: the ratio of reducing valences to oxidizing valences in redox systems. *Catalysis Science & Technology*, *6*(21), 7800–7811. https://doi.org/10.1039/C6CY01603K

Gunawan, A. A., Wills, A., Mkhoyan, A., Thomas, M. G., & Norris, D. J. (2012). Imaging 'Invisible' Dopant Atoms in Semiconductor Nanocrystals. *Microscopy and Microanalysis*, *18*(S2), 298–299. https://doi.org/10.1017/S1431927612003340

Gusain, R., Kumar, N., & Ray, S. S. (2020). Factors Influencing the Photocatalytic Activity of Photocatalysts in Wastewater Treatment. *Photocatalysts in Advanced Oxidation Processes for Wastewater Treatment*, 229–270. https://doi.org/10.1002/9781119631422.ch8

Hedaoo, M. N., Bhole, A. G., Ingole, N. W., & Hung, Y. T. (2012). Biological wastewater treatment. *Handbook of Environment and Waste Management: Air and Water Pollution Control*, 431–473. https://doi.org/10.1142/9789814327701_0012

Holkar, C. R., Jadhav, A. J., Pinjari, D. V., Mahamuni, N. M., & Pandit, A. B. (2016). A critical review on textile wastewater treatments: Possible approaches. *Journal of Environmental Management*, *182*, 351–366. https://doi.org/10.1016/j.jenvman.2016.07.090

Hong, R. Y., Li, J. H., Chen, L. L., Liu, D. Q., Li, H. Z., Zheng, Y., & Ding, J. (2009). Synthesis, surface modification and photocatalytic property of ZnO nanoparticles. *Powder Technology*, *189*(3), 426–432. https://doi.org/10.1016/j.powtec.2008.07.004

Hotze, E. M., Phenrat, T., & Lowry, G. V. (2010). Nanoparticle Aggregation: Challenges to Understanding Transport and Reactivity in the Environment. *Journal of Environmental Quality*, *39*(6), 1909–1924. https://doi.org/10.2134/jeq2009.0462

Huang, C.-Y., Hu, K.-H., & Wei, Z.-H. (2016). Comparison of cell behavior on pva/pva-gelatin electrospun nanofibers with random and aligned configuration. *Scientific Reports*, *6*(1), 37960. https://doi.org/10.1038/srep37960

Irani, M., Mohammadi, T., & Mohebbi, S. (2016). Photocatalytic degradation of methylene blue with zno nanoparticles; a joint experimental and theoretical study. *Journal of the Mexican Chemical Society*, *60*(4), 218–225. https://doi.org/10.29356/jmcs.v60i4.115

Islah-u-din, Salam, W. T., Gillani, S. S. A., Tahir, M. B., Ikram, M., & Ali, S. (2020). Tuning the structure and optical properties of nanostructured CdS by Cu doping. *Optik*, *203*, 163966. https://doi.org/10.1016/j.ijleo.2019.163966

Jiamprasertboon, A., Kafizas, A., Sachs, M., Ling, M., Alotaibi, A. M., Lu, Y., Siritanon, T., Parkin, I. P., & Carmalt, C. J. (2019). Heterojunction α-Fe 2 O 3 /ZnO Films with Enhanced Photocatalytic Properties Grown by Aerosol-Assisted Chemical Vapour Deposition. *Chemistry – A European Journal*, chem.201902175.

https://doi.org/10.1002/chem.201902175

Joshi, N. C., Gururani, P., & Gairola, S. P. (2022). Metal oxide nanoparticles and their nanocomposite-based materials as photocatalysts in the degradation of dyes. *Biointerface Research in Applied Chemistry*, *12*(5), 6557–6579. https://doi.org/10.33263/BRIAC125.65576579

Katheresan, V., Kansedo, J., & Lau, S. Y. (2018). Efficiency of various recent wastewater dye removal methods: A review. *Journal of Environmental Chemical Engineering*, *6*(4), 4676–4697. https://doi.org/10.1016/j.jece.2018.06.060

Kazmi, J., Ooi, P. C., Raza, S. R. A., Goh, B. T., Karim, S. S. A., Samat, M. H., Lee, M. K., Mohd. Razip Wee, M. F., Taib, M. F. M., & Mohamed, M. A. (2021). Appealing stable room-temperature ferromagnetism by well-aligned 1D Co-doped zinc oxide nanowires. *Journal of Alloys and Compounds*, *872*, 159741. https://doi.org/10.1016/j.jallcom.2021.159741

Khan, H., Habib, M., Khan, A., & Boffito, D. C. (2020). A modified sol-gel synthesis to yield a stable Fe3+/ZnO photocatalyst: Degradation of water pollutants and mechanistic insights under UV and visible light. *Journal of Environmental Chemical Engineering*, *8*(5), 104282. https://doi.org/10.1016/j.jece.2020.104282

Kolodziejczak-Radzimska, A., & Jesionowski, T. (2014). Zinc oxide-from synthesis to application: A review. *Materials*, *7*(4), 2833–2881. https://doi.org/10.3390/ma7042833

Kong, X., Zhu, H., Chen, C., Huang, G., & Chen, Q. (2017). Insights into the reduction of 4-nitrophenol to 4-aminophenol on catalysts. *Chemical Physics Letters*, *684*, 148–152. https://doi.org/10.1016/j.cplett.2017.06.049

Kowsari, E. (2017). *Carbon-Based Nanocomposites for Visible Light-Induced Photocatalysis*. https://doi.org/10.1007/978-3-319-62446-4_8

Kumar, A., & Choudhury, R. (2018). Eco-friendly dyes and dyeing , You may download the paper from the following link : http://sciedtech.eu/journals/advmtenvsci/current-issue/ ECO-FRIENDLY DYES AND DYEING. *Advanced Materials and Technologiies for Environmental Applications*, *2*(April), 145–176.

Kuriakose, S., Satpati, B., & Mohapatra, S. (2015). Highly efficient photocatalytic degradation of organic dyes by Cu doped ZnO nanostructures. *Physical Chemistry Chemical Physics*, *17*(38), 25172–25181. https://doi.org/10.1039/c5cp01681a

Lachheb, H., Ajala, F., Hamrouni, A., Houas, A., Parrino, F., & Palmisano, L. (2017). Electron transfer in ZnO–Fe 2 O 3 aqueous slurry systems and its effects on visible light photocatalytic activity. *Catalysis Science & Technology*, *7*(18), 4041–4047. https://doi.org/10.1039/C7CY01085K

Lan, L., Gnappi, G., & Montenero, A. (1993). Infrared study of EPOXS-TEOS-TPOT gels. *Journal of Materials Science*, *28*(8), 2119–2123. https://doi.org/10.1007/BF00367571

Lazarova, T., Georgieva, M., Tzankov, D., Voykova, D., Aleksandrov, L., Cherkezova-Zheleva, Z., & Kovacheva, D. (2017). Influence of the type of fuel used for the solution combustion synthesis on the structure, morphology and magnetic properties of nanosized NiFe2O4. *Journal of Alloys and Compounds*, *700*, 272–283. https://doi.org/10.1016/j.jallcom.2017.01.055

Liu, B., You, Y., Zhang, H., Wu, H., Jin, J., & Liu, H. (2016). Synthesis of ZnO nano-powders via a novel PVA-assisted freeze-drying process. *RSC Advances*, *6*(111), 110349–110355. https://doi.org/10.1039/C6RA24154A

Liu, X., Si, W., Zhang, J., Sun, X., Deng, J., Baunack, S., Oswald, S., Liu, L., Yan, C., & Schmidt, O. G. (2014). Free-standing Fe2O3 nanomembranes enabling ultra-long cycling life and high rate capability for Li-ion batteries. *Scientific Reports*, *4*(1), 7452. https://doi.org/10.1038/srep07452

Ludi, B., & Niederberger, M. (2013). Zinc oxide nanoparticles: Chemical mechanisms and classical and non-classical crystallization. *Dalton Transactions*, *42*(35), 12554–12568. https://doi.org/10.1039/c3dt50610j

Lupan, O., Ababii, N., Mishra, A. K., Gronenberg, O., Vahl, A., Schürmann, U., Duppel, V., Krüger, H., Chow, L., Kienle, L., Faupel, F., Adelung, R., de Leeuw, N. H., & Hansen, S. (2020). Single CuO/Cu 2 O/Cu Microwire Covered by a Nanowire Network as a Gas Sensor for the Detection of Battery Hazards. *ACS Applied Materials & Interfaces*, *12*(37), 42248–42263. https://doi.org/10.1021/acsami.0c09879

Ma, Q., Yang, X., Lv, X., Jia, H., & Wang, Y. (2019). Cu doped ZnO hierarchical nanostructures: morphological evolution and photocatalytic property. *Journal of Materials Science: Materials in Electronics*, *30*(3), 2309–2315. https://doi.org/10.1007/s10854-018-0503-1

Mahmoud, A., Echabaane, M., Omri, K., Boudon, J., Saviot, L., Millot, N., & Chaabane, R. Ben. (2021). Cu-doped ZnO nanoparticles for non-enzymatic glucose sensing. *Molecules*, *26*(4). https://doi.org/10.3390/molecules26040929

Majeed Khan, M. A., Siwach, R., Kumar, S., Ahmed, M., & Ahmed, J. (2020). Investigations on microstructure, optical, magnetic, photocatalytic, and dielectric behaviours of pure and Co-doped ZnO NPs. *Journal of Materials Science: Materials in Electronics*, *31*(8), 6360–6371. https://doi.org/10.1007/s10854-020-03192-2

Mejía, Y. R., & Reddy Bogireddy, N. K. (2022). Reduction of 4-nitrophenol using green-fabricated metal nanoparticles. *RSC Advances*, *12*(29), 18661–18675. https://doi.org/10.1039/D2RA02663E

Mitchell, S., Qin, R., Zheng, N., & Pérez-Ramírez, J. (2021). Nanoscale engineering of catalytic materials for sustainable technologies. *Nature Nanotechnology*, *16*(2), 129–139. https://doi.org/10.1038/s41565-020-00799-8

Mittal, M., Sharma, M., & Pandey, O. P. (2014). UV-Visible light induced photocatalytic studies of Cu doped ZnO nanoparticles prepared by co-precipitation method. *Solar Energy*, *110*, 386–397. https://doi.org/10.1016/j.solener.2014.09.026

Mohd Adnan, M. A., Julkapli, N. M., & Abd Hamid, S. B. (2016). Review on ZnO hybrid photocatalyst: impact on photocatalytic activities of water pollutant degradation. *Reviews in Inorganic Chemistry*, *36*(2), 77–104. https://doi.org/10.1515/revic-2015-0015

Mojsov, K. D., Andronikov, D., Janevski, A., Kuzelov, A., & Gaber, S. (2016). The Application of Enzymes for the Removal of Dyes From. *Advanced Technologies*, *5*(1), 81–86.

Morales-Mendoza, J. E., & Paraguay-Delgado, F. (2021). Widening UV–Vis absorption band by Cu doped ZnO and ZnO/CuO composite. *Materials Letters*, *291*, 129494. https://doi.org/10.1016/j.matlet.2021.129494

Nadeem, M. S., Munawar, T., Mukhtar, F., Naveed ur Rahman, M., Riaz, M., & Iqbal, F. (2021). Enhancement in the photocatalytic and antimicrobial properties of ZnO nanoparticles by structural variations and energy bandgap tuning through Fe and Co co-doping. *Ceramics International*, *47*(8), 11109–11121. https://doi.org/10.1016/j.ceramint.2020.12.234

Nadupalli, S., Repp, S., Weber, S., & Erdem, E. (2021). About defect phenomena in ZnO nanocrystals. *Nanoscale*, *13*(20), 9160–9171. https://doi.org/10.1039/D1NR00943E

Naseer, S., Aamir, M., Mirza, M. A., Jabeen, U., Tahir, R., Malghani, M. N. K., & Wali, Q. (2022). Synthesis of Ni–Ag–ZnO solid solution nanoparticles for photoreduction and antimicrobial applications. *RSC Advances*, *12*(13), 7661–7670. https://doi.org/10.1039/D2RA00717G

Novitskaya, E., Kelly, J. P., Bhaduri, S., & Graeve, O. A. (2021). A review of solution combustion synthesis: an analysis of parameters controlling powder characteristics. *International Materials Reviews*, *66*(3), 188–214. https://doi.org/10.1080/09506608.2020.1765603

Özgür, Ü., Avrutin, V., & Morkoç, H. (2018). Zinc Oxide Materials and Devices Grown by Molecular Beam Epitaxy. In *Molecular Beam Epitaxy*. https://doi.org/10.1016/b978-0-12-812136-8.00016-5

Paraguay-Delgado, F., Hermida-Montero, L. A., Morales-Mendoza, J. E., Durán-Barradas, Z., Mtz-Enriquez, A. I., & Pariona, N. (2022). Photocatalytic properties of Cu-containing ZnO nanoparticles and their antifungal activity against agriculture-pathogenic fungus. *RSC Advances*, *12*(16), 9898–9908. https://doi.org/10.1039/D2RA00863G

Park, J. C., Kim, A. Y., Kim, J. Y., Park, S., Park, K. H., & Song, H. (2012). ZnO–CuO core–branch nanocatalysts for ultrasound-assisted azide–alkyne cycloaddition reactions. *Chemical Communications*, *48*(68), 8484. https://doi.org/10.1039/c2cc31654d

Pirhashemi, M., Habibi-Yangjeh, A., & Rahim Pouran, S. (2018). Review on the criteria anticipated for the fabrication of highly efficient ZnO-based visible-light-driven photocatalysts. *Journal of Industrial and Engineering Chemistry*, *62*, 1–25.

https://doi.org/10.1016/j.jiec.2018.01.012

Polte, J. (2015). Fundamental growth principles of colloidal metal nanoparticles - a new perspective. *CrystEngComm*, *17*(36), 6809–6830. https://doi.org/10.1039/c5ce01014d

Prabakaran, E., & Pillay, K. (2019). Synthesis of N-doped ZnO nanoparticles with cabbage morphology as a catalyst for the efficient photocatalytic degradation of methylene blue under UV and visible light. *RSC Advances*, *9*(13), 7509–7535. https://doi.org/10.1039/C8RA09962F

Radhamani, A. V., Shareef, K. M., & Rao, M. S. R. (2016). ZnO@MnO2 Core-Shell Nanofiber Cathodes for High Performance Asymmetric Supercapacitors. *ACS Applied Materials and Interfaces*, *8*(44), 30531–30542. https://doi.org/10.1021/acsami.6b08082

Rafeeq, H., Hussain, A., Ambreen, A., Zill-e-Huma, Waqas, M., Bilal, M., & Iqbal, H. M. N. (2022). Functionalized nanoparticles and their environmental remediation potential: a review. *Journal of Nanostructure in Chemistry*, *12*(6), 1007–1031. https://doi.org/10.1007/s40097-021-00468-9

Ray, C., Dutta, S., Sarkar, S., Sahoo, R., Roy, A., & Pal, T. (2013). A facile synthesis of 1D nano structured selenium and Au decorated nano selenium: Catalysts for the clock reaction. *RSC Advances*, *3*(46), 24313. https://doi.org/10.1039/c3ra44102d

Robinson, T., McMullan, G., Marchant, R., & Nigam, P. (2001). Remediation of dyes in textile effluent: A critical review on current treatment technologies with a proposed alternative. *Bioresource Technology*, *77*(3), 247–255. https://doi.org/10.1016/S0960-8524(00)00080-8

Rossell, M. D., Ramasse, Q. M., Findlay, S. D., Rechberger, F., Erni, R., & Niederberger, M. (2012). Direct Imaging of Dopant Clustering in Metal–Oxide Nanoparticles. *ACS Nano*, *6*(8), 7077–7083. https://doi.org/10.1021/nn3021212

Saggioro, E. M., Oliveira, A. S., Pavesi, T., Maia, C. G., Ferreira, L. F. V., & Moreira, J. C. (2011). Use of titanium dioxide photocatalysis on the remediation of model textile wastewaters containing azo dyes. *Molecules*, *16*(12), 10370–10386. https://doi.org/10.3390/molecules161210370

Samanta, A., Goswami, M. N., & Mahapatra, P. K. (2020). Fe-doped ZnO nanoparticles as novel photonic and multiferroic semiconductor. *Materials Chemistry and Physics*, *240*(August 2019), 122180. https://doi.org/10.1016/j.matchemphys.2019.122180

Samsami, S., Mohamadi, M., Sarrafzadeh, M. H., Rene, E. R., & Firoozbahr, M. (2020). Recent advances in the treatment of dye-containing wastewater from textile industries: Overview and perspectives. *Process Safety and Environmental Protection*, *143*, 138–163. https://doi.org/10.1016/j.psep.2020.05.034

Sanakousar, F. M., Vidyasagar, C., Jiménez-Pérez, V. M., & Prakash, K. (2022). Recent progress on visible-light-driven metal and non-metal doped ZnO nanostructures for photocatalytic degradation of organic pollutants. *Materials Science in Semiconductor*

Processing, *140*(November 2021). https://doi.org/10.1016/j.mssp.2021.106390

Schneider, K. (2020). Optical properties and electronic structure of V2O5, V2O3 and VO2. *Journal of Materials Science: Materials in Electronics*, *31*(13), 10478–10488. https://doi.org/10.1007/s10854-020-03596-0

Selvi, J., Mahalakshmi, S., Parthasarathy, V., Hu, C., Lin, Y., Tung, K., Anbarasan, R., & Annie, A. A. (2019). Optical, thermal, mechanical properties, and non-isothermal degradation kinetic studies on PVA/CuO nanocomposites. *Polymer Composites*, *40*(9), 3737–3748. https://doi.org/10.1002/pc.25235

Senobari, S., & Nezamzadeh-Ejhieh, A. (2020). A novel ternary nano-composite with a high photocatalyitic activity: Characterization, effect of calcination temperature and designing the experiments. *Journal of Photochemistry and Photobiology A: Chemistry*, *394*(November 2019), 112455. https://doi.org/10.1016/j.jphotochem.2020.112455

Sharma, D., & Jha, R. (2017). Analysis of structural, optical and magnetic properties of Fe/Co co-doped ZnO nanocrystals. *Ceramics International*, *43*(11), 8488–8496. https://doi.org/10.1016/j.ceramint.2017.03.201

Sharma, P., & Qanungo, K. (2022). *Challenges in Effluents Treatment Containing Dyes Advance Research in Textile Engineering Challenges in Effluents Treatment Containing Dyes*. *December*.

Shim, J. H., Hwang, T., Lee, S., Park, J. H., Han, S.-J., & Jeong, Y. H. (2005). Origin of ferromagnetism in Fe- and Cu-codoped ZnO. *Applied Physics Letters*, *86*(8), 082503. https://doi.org/10.1063/1.1868872

Siddique, F., & Gonzalez-cortes, S. (2022). *Solution combustion synthesis : the relevant metrics for producing advanced and*. 1–7. https://doi.org/10.1039/d2nr02714c

Sivakumar, P., Ramesh, R., Ramanand, A., Ponnusamy, S., & Muthamizhchelvan, C. (2011). Preparation and properties of nickel ferrite (NiFe2O 4) nanoparticles via sol-gel auto-combustion method. *Materials Research Bulletin*, *46*(12), 2204–2207. https://doi.org/10.1016/j.materresbull.2011.09.010

Soleimani, H., Baig, M. K., Yahya, N., Khodapanah, L., Sabet, M., Demiral, B. M. R., & Burda, M. (2018). Synthesis of ZnO nanoparticles for oil–water interfacial tension reduction in enhanced oil recovery. *Applied Physics A: Materials Science and Processing*, *124*(2), 0. https://doi.org/10.1007/s00339-017-1510-4

Subash, B., Krishnakumar, B., Velmurugan, R., Swaminathan, M., & Shanthi, M. (2012). Synthesis of Ce co-doped Ag–ZnO photocatalyst with excellent performance for NBB dye degradation under natural sunlight illumination. *Catalysis Science & Technology*, *2*(11), 2319. https://doi.org/10.1039/c2cy20254a

Sudha, M., Senthilkumar, S., Hariharan, R., Suganthi, A., & Rajarajan, M. (2012). Controlled reduction of the deleterious effects of photocatalytic activity of ZnO nanoparticles by PVA capping. *Journal of Sol-Gel Science and Technology*, *61*(1), 14–22. https://doi.org/10.1007/s10971-011-2584-7

Thoda, O., Xanthopoulou, G., Vekinis, G., & Chroneos, A. (2018). Review of Recent Studies on Solution Combustion Synthesis of Nanostructured Catalysts. *Advanced Engineering Materials*, *20*(8), 1800047. https://doi.org/10.1002/adem.201800047

Tian, S., Liu, Q., Sun, J., Zhu, M., Wu, S., & Zhao, X. (2019). Mesoporous ZnO nanorods array with a controllable area density for enhanced photocatalytic properties. *Journal of Colloid and Interface Science*, *534*, 389–398. https://doi.org/10.1016/j.jcis.2018.09.049

Tiwari, N., Lohar, A., Kamal, C., Chakrabarti, A., Prajapat, C. L., Mishra, P. K., Mondal, P., Karnar, B., Misra, N. L., Jha, S. N., & Bhattacharyya, D. (2017). Structural and magnetic studies on (Fe, Cu) co-doped ZnO nanocrystals. *Journal of Physics and Chemistry of Solids*, *104*, 198–206. https://doi.org/10.1016/j.jpcs.2017.01.023

Tsogoo, A., Tsedev, N., Gibaud, A., Daniel, P., Kassiba, A., Fukuda, M., Kusano, Y., Azuma, M., Tsogbadrakh, N., Ragchaa, G., Dashzeveg, R., & Ganbold, E.-O. (2023). Experimental and ab initio studies on the structural, magnetic, photocatalytic, and antibacterial properties of Cu-doped ZnO nanoparticles. *RSC Advances*, *13*(2), 1256–1266. https://doi.org/10.1039/D2RA07204A

Tulinski, M., & Jurczyk, M. (2017). Nanomaterials Synthesis Methods. *Metrology and Standardization of Nanotechnology*, *1*, 75–98. https://doi.org/10.1002/9783527800308.ch4

Uthirakumar, P., Devendiran, M., Kim, T. H., Kalaiarasan, S., & Lee, I.-H. (2020). Fabrication of flexible sheets of Cu/CuO/Cu2O heterojunction nanodisks: A dominant performance of multiple photocatalytic sheets under natural sunlight. *Materials Science and Engineering: B*, *260*(March), 114652. https://doi.org/10.1016/j.mseb.2020.114652

Varma, A., Mukasyan, A. S., Rogachev, A. S., & Manukyan, K. V. (2016). Solution Combustion Synthesis of Nanoscale Materials. *Chemical Reviews*, *116*(23), 14493–14586. https://doi.org/10.1021/acs.chemrev.6b00279

Viswanatha, R., Naveh, D., Chelikowsky, J. R., Kronik, L., & Sarma, D. D. (2012). Magnetic Properties of Fe/Cu Codoped ZnO Nanocrystals. *The Journal of Physical Chemistry Letters*, *3*(15), 2009–2014. https://doi.org/10.1021/jz300741z

Wang, J., Cao, J., Fang, B., Lu, P., Deng, S., & Wang, H. (2005). Synthesis and characterization of multipod, flower-like, and shuttle-like ZnO frameworks in ionic liquids. *Materials Letters*, *59*(11), 1405–1408. https://doi.org/10.1016/j.matlet.2004.11.062

Wang, Z., Su, R., Wang, D., Shi, J., Wang, J.-X., Pu, Y., & Chen, J.-F. (2017). Sulfurized Graphene as Efficient Metal-Free Catalysts for Reduction of 4-Nitrophenol to 4-Aminophenol. *Industrial & Engineering Chemistry Research*, *56*(46), 13610–13617. https://doi.org/10.1021/acs.iecr.7b03217

Xu, K., Wu, J., Tan, C. F., Ho, G. W., Wei, A., & Hong, M. (2017). Ag–CuO–ZnO metal–semiconductor multiconcentric nanotubes for achieving superior and perdurable

photodegradation. *Nanoscale*, *9*(32), 11574–11583. https://doi.org/10.1039/C7NR03279J

Xu, M., Chen, Y., Hu, W. Y., Liu, Y. T., Zhang, Q. P., Yuan, H., Wang, X. Y., Zhang, J. X., Luo, K. Y., Li, J., & Xiong, G. (2020). Designed synthesis of microstructure and defect-controlled Cu-doped ZnO–Ag nanoparticles: exploring high-efficiency sunlight-driven photocatalysts. *Journal of Physics D: Applied Physics*, *53*(2), 025106. https://doi.org/10.1088/1361-6463/ab4bfd

Yang, Z., Zong, X. L., Ye, Z., Zhao, B., Wang, Q. L., & Wang, P. (2010). The application of complex multiple forklike ZnO nanostructures to rapid and ultrahigh sensitive hydrogen peroxide biosensors. *Biomaterials*, *31*(29), 7534–7541. https://doi.org/10.1016/j.biomaterials.2010.06.019

Zaid, H. M., Adil, M., & Lee, K. C. (2017). Structural and morphological evolution of metal oxide nanoparticles synthesised via sol-gel auto-combustion. *International Journal of Nanotechnology*, *14*(1–6), 284–296. https://doi.org/10.1504/IJNT.2017.082478

Zangeneh, H., Zinatizadeh, A. A. L., Habibi, M., Akia, M., & Hasnain Isa, M. (2015). Photocatalytic oxidation of organic dyes and pollutants in wastewater using different modified titanium dioxides: A comparative review. *Journal of Industrial and Engineering Chemistry*, *26*, 1–36. https://doi.org/10.1016/j.jiec.2014.10.043

Zhao, Y., Deng, C., Tang, D., Ding, L., Zhang, Y., Sheng, H., Ji, H., Song, W., Ma, W., Chen, C., & Zhao, J. (2021). α-Fe2O3 as a versatile and efficient oxygen atom transfer catalyst in combination with H2O as the oxygen source. *Nature Catalysis*, *4*(8), 684–691. https://doi.org/10.1038/s41929-021-00659-1

Zverev, A. S., Ilyakova, N. N., Nurmukhametov, D. R., Dudnikova, Y. N., Russakov, D. M., Pugachev, V. M., & Mitrofanov, A. Y. (2022). Iron and Copper Doped Zinc Oxide Nanopowders as a Sensitizer of Industrial Energetic Materials to Visible Laser Radiation. *Nanomaterials*, *12*(23), 4176. https://doi.org/10.3390/nano12234176

Research Fund Acknowledgement

This research thesis was funded by Adama Science and Technology University under the grant number of ASTU/SM-R/691/23, Adama, Ethiopia.